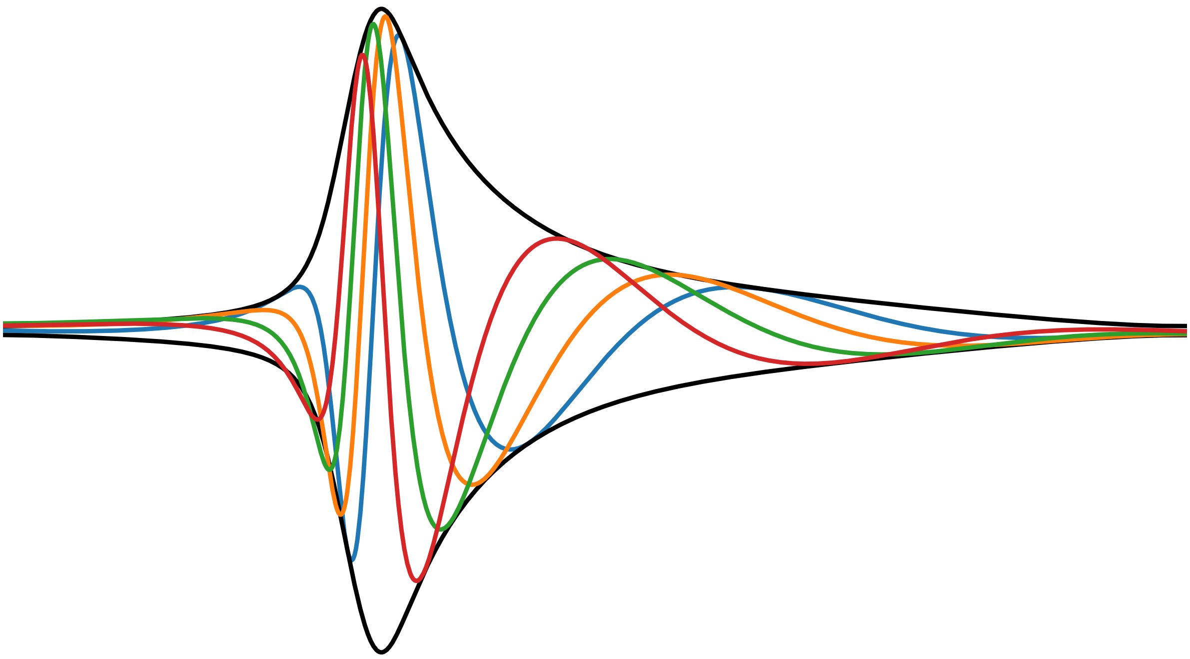

Models of sub-cycle electromagnetic pulse generation in laser-plasma interaction

Master's thesis in Physics and Astronomy

CHRISTOFFER OLOFSSON

Department of Physics
CHALMERS UNIVERSITY OF TECHNOLOGY
Gothenburg, Sweden 2020

Master's thesis 2020:TIFX05

Models of sub-cycle electromagnetic pulse generation in laser-plasma interaction

CHRISTOFFER OLOFSSON

Department of Physics
Division of Subatomic, High Energy and Plasma Physics
Chalmers University of Technology
Gothenburg, Sweden 2020

Models of sub-cycle electromagnetic pulse generation in laser-plasma interaction
CHRISTOFFER OLOFSSON

Supervisor: Evangelos Siminos, Department of Physics, University of Gothenburg
Examiner: Tünde Fülöp, Department of Physics

Master's Thesis 2020:TIFX05
Department of Physics
Division of Subatomic, High Energy and Plasma Physics
Chalmers University of Technology
SE-412 96 Gothenburg
Telephone +46 31 772 1000

Cover: Demonstration of CEP tunability of the sub-cycle pulse with respect to the seed phase. For an in-depth explanation please examine figure 4.11 in section 4.3.

Typeset in LaTeX
Printed by Chalmers Reproservice
Gothenburg, Sweden 2020

Models of sub-cycle electromagnetic pulse generation in laser-plasma interaction
CHRISTOFFER OLOFSSON
Department of Physics
Chalmers University of Technology

Abstract

Sub-cycle pulses are ultra-short laser pulses containing less than a single oscillation and are essential tools in the study of matter at the shortest timescales. It has been recently proposed that such pulses can be attained by letting laser pulses interact with a plasma to generate amplified and compressed pulses. In the scheme of laser wakefield driven amplification (LWDA), an initial seed pulse is modulated by traveling electron plasma waves, forming amplified sub-cycle pulses. In this thesis we investigate the underlying mechanism of sub-cycle pulse generation in the scheme of LWDA. An analytical approach using the method of Green's functions is used in conjunction with particle-in-cell simulations. Moreover, a custom code solving Maxwell's equations with a source term given by a non-linear plasma wave model is implemented and its results compared with particle-in-cell simulations.

Keywords: laser, plasma, ultra-short, non-linear, wakefield, sub-cycle, optics

Acknowledgements

First and foremost I would like to express my enormous gratitude towards my supervisor Evangelos Siminos. He was the one who introduced me to the vast field of laser-plasma physics, providing me with many topics to be explored for a master's thesis. Not only has he supported me with brilliant ideas for the thesis, but he has always been there to answer questions, provide research material and give guidance no matter what the circumstances are. I would also like to thank Tünde Fülöp for giving me a very warm and positive welcome to the research group and taking her time to examine my thesis. She has made sure I have everything I need and always lightens up the mood.

Lastly, I would like to express my gratitude towards the research group as a whole. I cannot include all of your names here but I appreciate every single one of you, having welcomed me to the group, provided excellent company for coffee breaks and much more.

Christoffer Olofsson, Gothenburg, June 2020

Contents

1

Introduction

Electromagnetic fields performing less than a single oscillation are commonly referred to as sub-cycle pulses and are invaluable tools when studying matter at the shortest timescales. Said pulses have a temporal duration of only a few-femtoseconds or even an attosecond which can be utilized to control and collide electron wavepackets in solids [1]. These generate high-harmonic radiation which in turn contains valuable information about the structure of atoms and molecules. Furthermore, with attosecond pulses it is also possible to render electron dynamics in real time since the electron motion, caused by the mutual influence of the electrons in an molecule or atom along with the nuclear potential happens on the attosecond scale [2].

One of the first approaches of producing short pulses was by mode-locking discovered in 1964 [2] and has been able to produce few-cycle pulses with durations below 10 fs [3]. Ever since, other methods to produce short pulses have been developed such as Optical Parametric Amplification (OPA) or optical synthesis [4]. However, these common ways of producing few-cycle pulses are susceptible to equipment damage as one is trying to scale the interaction to high intensities [5]. As an alternative, it is possible to make use of a plasma or electron beams as a generating medium. A plasma is an ionized gas consisting of ions and electrons which in this sense has already undergone ionization damage and is a viable option for sub-cycle pulse generation at very high intensities. Electromagnetic fields and plasmas exhibit a wide range of phenomena already and the ability for the plasma to amplify and shorten laser pulses are well-known.

One seemingly simple approach to achieve sub-cycle fields is to let incident radiation impinge on a dense plasma which can produce various reflected harmonics which is known as high harmonic generation (HHG). In the work of [6], [7] and [8], electromagnetic radiation is incident normally onto a dense plasma and reflected subfemtosecond pulses is returned in the form of pulse trains. Another interesting example of this is *coherent synchrotron emission* (CSE) which was treated in [9], [10] and [11]. In this framework, the principle is that a few-cycle pulse is obliquely incident onto an overdense plasma in the ultrarelativistic regime which produce ultrathin electron layers at the plasma boundary. These layers are referred to as *nanobunches* and emit attosecond radiation coherently. A difference between the two schemes is that in the latter case it is possible to yield an isolated sub-cycle pulse instead of a pulse train due to the cycles contained in the driving laser. Thus it should be stressed that in order to yield isolated sub-cycle pulses, also single-cycle driving fields are needed which is technically demanding [12]. Other means to isolate a single pulse can be achieved by spectral filtering [13] or polarization gating [14].

Two other interesting setups employing plasma based sub-cycle pulse generation is electron beam driven amplification (EBDA) [5] which relies on the interaction between a short electron beam with a standing wave and laser wakefield driven amplification (LWDA) [15] employing non-linear electron plasma waves to modulate a seed electromagnetic field. Both EBDA and LWDA are relevant to this thesis but the focus will be put on LWDA. More specifically, in the arrangement of LWDA, a seed laser pulse will interact with non-linear plasma waves which has been excited by a high-intensity, co-propagating laser pulse within a plasma. This has shown to produce intense, isolated sub-cycle pulses with the possibility to tune their carrier-envelope phase (CEP). This means that the issue of using single-cycle driving lasers to generate isolated sub-cycle fields can be overcome. In addition to this, isolated, CEP-stable pulses are very desirable as they have applications in solid-state physics [16] but also in nano-engineering [17].

As mentioned, both EBDA and LWDA make use of electron pulses with short dimensions in order to modulate the seed beam into sub-cycle pulses, meaning that there ought to be a common theoretical description linking them together. So far the schemes of EBDA and LWDA have only been investigated numerically and have been modeled by a qualitative analytical theory. To this day there does not exist a common theory that can make quantitative predictions for the sub-cycle radiation emitted in these frames. In this thesis, an attempt to develop such a theory in one dimension will be made by utilizing analytical tools which have been used in the study of ultra-intense HHG [9]. In addition to this, simulations employing the particle-in-cell (PIC) approach will be applied to the setup of LWDA in 1D in order to compare results of the theory but also further investigate the underlying mechanism of the sub-cycle pulse generation. Another procedure in unveiling the quantitative understanding towards LWDA will also be by applying a custom code solving Maxwell's equations. This code will be using the finite-difference time-domain (FDTD) method in conjunction with a theoretical model for non-linear plasma wake formation to simulate the interaction of LWDA. This has the potential to tailor the plasma properties which will help the investigation of the problem.

2

Theory

The relevant theory required in order to fully understand the analytical description behind sub-cycle pulse generation and simulation procedures will be found here. This chapter begins by introducing basic concepts of laser-plasma theory and explains how a plasma can be described macroscopically by both the kinetic and cold fluid description. In section 2.2 the numerical PIC approach is introduced, explaining the physics it implements and its numerical routines. Lastly, in section 2.3 the setup of LWDA is thoroughly discussed along with the qualitative theory it comes with.

2.1 Laser plasma theory

A plasma, commonly known as the fourth state of matter is an ionized gas consisting of electrons and ions. Although plasma appears to be an exotic state of matter, it is believed that 99% of our universe is composed of it [18]. This state can be found on our Earth in the shape of lightning strikes, welding arcs but also inside magnetic fusion devices. Plasmas can also be found in our Solar system in the form of solar winds and solar flares. In our Galaxy, a common example where to find plasma would be inside the galactic spiral arms. Due to the wide range of areas where plasmas can be observed, understanding this exotic state of matter is of utmost importance. A class of important applications is related to exploiting the properties of plasmas interacting with electromagnetic fields. By laser-plasma interaction it is possible to generate short, intense electromagnetic pulses. Such pulses can in some cases be generated in order to perform only one optical oscillation (single-cycle pulse) or even less than one oscillation (sub-cycle pulse). In this thesis it will be interesting to investigate one such scheme in particular. This method is referred to as Laser Wakefield Driven Amplification (LWDA) [15] and will be described in detail later on. For now it is important to give some basic laser plasma theory and present the equations which govern the underlying physics.

2.1.1 A brief note on plasma units

In this thesis, dimensionless and normalized units will be used in order to improve readability of the equations. As a starting point, charges are normalized to the fundamental charge, e. As an example, the charge of an electron, q_e would be written as $q_e = -1$ and not $q_e = -e$. In addition, all masses and velocities are measured in units of the electron rest mass, m_e and speed of light, c respectively.

Reference quantity	Reference value
Momentum, p_r	$m_e c$
Energy, K_r	$m_e c^2$
Time, T_r	$1/\omega_r$
Length, L_r	c/ω_r
Electric field, E_r	$\omega_r m_e c/e$
Magnetic field, B_r	$\omega_r m_e c/e$
Particle density, n_r	$m_e \epsilon_0 \omega_r^2/e^2$
Current, J_r	$m_e c \epsilon_0 \omega_r^2/e$

Table 2.1: A table containing the reference quantities relevant to this thesis, ϵ_0 is the vacuum permittivity of free space.

From this it is now possible to form more quantities which can be used for normalization such as a reference energy $K_r = m_e c^2$ and a reference momentum $p_r = m_e c$. Units are further normalized to some relevant quantity of the laser-plasma interaction such as a typical length scale or frequency of the problem. In this work it will be the frequency of a laser pulse used in the interaction that will be investigated. If this frequency is denoted ω_r, even more reference quantities can be constructed. All of the reference values are given by table 2.1. In the end, it is always possible to switch back to dimensional units when calculations are finished.

2.1.2 Basic plasma physics

In general, a plasma and its ability to couple to electromagnetic fields has the potential to display a vast number of different phenomena. In this section some of the more familiar and often used physical effects will be discussed. A good starting point is to consider how a plasma can screen out changes in electric potential which is commonly known as Debye screening [18]. Here we omit the calculation but the result can be extracted by the Poisson equation for a neutral plasma following a Boltzmann distribution along with an additional "test charge". One finds that the electrostatic potential (in spherically symmetric coordinates) is proportional to

$$\phi(r) \sim \frac{e^{-r/\lambda_D}}{r} \tag{2.1}$$

where $\lambda_D = \sqrt{\frac{T_e}{n_e}}$ is the Debye length. This means that for $r > \lambda_D$, the plasma effectively blocks the vacuum potential. In other words, any charge separation will induce some electromagnetic field that the neighboring charged particles will respond to. They will arrange themselves in such a manner as to erase this field and remain quasi-neutral. Quasi-neutral means that the plasma is only neutral when considered on a macroscopic scale. Only when observing the plasma on a scale $d \lesssim \lambda_D$ the charge separation will become apparent. For a non-collisional plasma, this action happens on a time-scale connected to the plasma frequency [19]. This is the typical oscillation frequency of displaced charged particles in a plasma. Usually, this is given as the electron plasma frequency as the ions can be treated as immobile due to their heavy mass compared to that of the "free" electrons and is written

$$\omega_{pe} = \sqrt{n_e} \tag{2.2}$$

where n_e is the number density of electrons.

Another useful result of the plasma response to electromagnetic fields is how its density can dictate whether an electromagnetic signal will propagate through it. To see this we first give the dispersion relation for electromagnetic fields propagating through a cold, non-magnetized, homogeneous plasma [20]

$$\omega^2 = \omega_{pe}^2 + k^2 \tag{2.3}$$

where ω is the angular frequency of the wave in question, ω_{pe} is the plasma frequency of the plasma and k is the wavenumber of the wave. It is easy to see that the wavenumber k can become imaginary in cases where $\omega < \omega_{pe}$ depending on the wave frequency and plasma density. This would imply that inside the plasma the field would be exponentially damped and if the slab of plasma is not extremely thin, the incoming wave will be totally reflected. On the contrary, if $\omega > \omega_{pe}$ waves will be transmitted through the plasma. An important quantity to define is a critical density, n_c, satisfying $\omega_{pe} = \omega$. From equation (2.2) one finds

$$n_c = \omega^2 \tag{2.4}$$

where again ω is the angular frequency of the wave. Now it is straightforward to see that i.e. no propagation takes place if $n_e > n_c$.

2.1.3 Maxwell's equations

Every electromagnetic field follows a set of equations known as Maxwell's equations. These equations encapsulate all electromagnetic phenomena, including their interaction with charges and are given as

$$\nabla \cdot \mathbf{E} = \rho \tag{2.5}$$

$$\nabla \times \mathbf{E} = -\frac{\partial \mathbf{B}}{\partial t} \tag{2.6}$$

$$\nabla \cdot \mathbf{B} = 0 \tag{2.7}$$

$$\nabla \times \mathbf{B} = (\mathbf{J} + \frac{\partial \mathbf{E}}{\partial t}) \tag{2.8}$$

where **E** is the electric field, **B** is the magnetic field[1], ρ is the charge density and **J** is the associated current density. Equation (2.5) is known as Gauss's law and describes e.g. how electric fields can be generated by distributions of charge. Maxwell-Faraday or simply Faraday's law is the frequently used name for equation (2.6) which explains how time-varying magnetic fields can give rise to electric fields. Equation (2.7) states that there exists no magnetic monopoles or put in other words : the absence of magnetic charges. Lastly there is Ampères law (equation (2.8)) which again states that a time-varying electric field may give rise to a magnetic field. In addition to this, distribution of charges in motion also produce magnetic field, hence the contribution of **J**.

---

[1] **B** is in fact the magnetic flux density but it is commonly referred to as the magnetic field.

2.1.4 Kinetic description of a plasma

So far we have discussed some basic properties of the plasma but not how to describe the plasma itself. To model the plasma as individual, charged particles is obviously too difficult as the number of particles is astronomically large in a plasma and the interaction is also coupled to Maxwell's equations. In addition to this, all charged particles within the plasma are interacting with each other via the Lorentz force equation given by

$$\mathbf{F}_{Lorentz} = q_i(\mathbf{E} + \mathbf{v} \times \mathbf{B}) \tag{2.9}$$

where q_i is the charge of the species in question and $\mathbf{v}$ is the instantaneous velocity of the particles. Again, $\mathbf{E}, \mathbf{B}$ are electromagnetic fields present within the plasma due to its constituent charge and potentially externally applied fields. Therefore it is necessary to adopt a statistical point of view known as a kinetic description of the plasma. In this framework, the relevant quantity in question will be the distribution function of the species within the plasma. Such a function, $f_i = f_i(\mathbf{r}, \mathbf{p}, t)$ gives the number of particles per unit volume located at a given position in phase space $(\mathbf{r}, \mathbf{p})$ and time, t where i denotes the species (e.g. e for electrons). Having information about the distribution function for each species in the system is enough for one to use the kinetic approach [18]. This is because when f_i is known, physical quantities can be constructed by taking "velocity moments" of the distribution f_i. An important example of this would be the total number density

$$n_i(\mathbf{r}, t) = \int f_i(\mathbf{r}, \mathbf{p}, t) d^3p \tag{2.10}$$

where the integration is over the whole of momentum space. This is referred to as a zeroth-order velocity moment since the integrand contains only f_i with a zeroth power of the velocity, $\mathbf{v}^0 = 1$. Another important quantity derived from a (first-order) velocity moment is the mean velocity

$$\mathbf{u}_i(\mathbf{r}, t) = \frac{1}{n_i} \int \mathbf{v} f_i(\mathbf{r}, \mathbf{p}, t) d^3p \tag{2.11}$$

where $\mathbf{v}$ can be expressed as $\mathbf{v} = \frac{\mathbf{p}}{m_i \gamma}$.

Lastly, it can be shown that the distributions, f_i satisfy the so called Vlasov equation which is used to determine f_i [18]

$$\Big(\frac{\partial}{\partial t} + \frac{\mathbf{p}}{m_i \gamma} \cdot \nabla_r + \frac{q_i}{m_i \gamma} (\mathbf{E} + \mathbf{p} \times \mathbf{B}) \cdot \nabla_p\Big) f_i = 0 \tag{2.12}$$

where m_i is the mass of a certain species, $\gamma = \sqrt{1 + \frac{\mathbf{p}^2}{m_i^2}}$ is the Lorentz factor and $\nabla_{r,p}$ denote differentiation with respect to space and momentum respectively. Thus, all electromagnetic fields are coupled to Maxwell's equations (2.5)-(2.8) and are produced by the total charge and current densities related to equation (2.10) and (2.11) via

$$\rho(\mathbf{r}, t) = \sum_i q_i n_i = \sum_i q_i \int f_i(\mathbf{r}, \mathbf{p}, t) d^3p \tag{2.13}$$

$$\mathbf{J}(\mathbf{r}, t) = \sum_i q_i n_i \mathbf{u}_i = \sum_i q_i \int \mathbf{v} f_i(\mathbf{r}, \mathbf{p}, t) d^3p. \tag{2.14}$$

These form together with the Lorentz force (2.9) and the Vlasov equation (2.12) a closed system of equations that governs the whole laser-plasma interaction.

2.1.5 Cold fluid description of a plasma

A different approach to model a plasma is through the fluid description where the plasma as a whole is treated as a single charged fluid or composed of several such fluids due to different particle species. As previously mentioned, the ions in this work are assumed to be stationary due to their heavy mass so that the plasma should be modeled by a single electron fluid with a neutralizing background.

Contrary to the kinetic description of working with the distribution function, f_i, velocity moments of the Vlasov equation (2.12) are computed [18]. This is done to yield equations governing the dynamics for the averaged quantities introduced in equations (2.10) and (2.11). It is possible to generate an infinite amount of equations and quantities which at some point has to be closed by an appropriate equation of state. Relevant to this thesis is the relativistic cold fluid description which has an equation of state corresponding to the temperature of the electrons being zero, i.e. neglecting thermal effects. However, it should be noted that the electrons are still able to attain relativistic momentum in this model from intense laser-plasma coupling. In order to arrive at the relativistic cold fluid equations the assumption of cold electrons implies an insignificant thermal spread which in turn means that the momentum distribution for them will be a Dirac delta distribution [20]. Then, introducing an average momentum, $\mathbf{p}$ similarly to equations (2.10) and (2.11) one obtains the relativistic cold fluid equations (in this case given for a single electron fluid)

$$\frac{\partial n_e}{\partial t} + \nabla \cdot (n_e \mathbf{u}) = 0 \tag{2.15}$$

$$\frac{d\mathbf{p}}{dt} = q_e(\mathbf{E} + \mathbf{u} \times \mathbf{B}) \tag{2.16}$$

$$\nabla^2 \phi = k_p^2 (n_e/n_0 - 1) \tag{2.17}$$

where $\frac{d}{dt} = \frac{\partial}{\partial t} + \mathbf{u} \cdot \nabla$, $\mathbf{p} = \gamma_e \mathbf{u}$ is the electron fluid momentum, $\mathbf{u}$ is the electron fluid velocity, ϕ is the electrostatic potential and n_0 is the ambient plasma density. Recall that n_e is the electron density and that the electron charge is $q_e = -1$. Equation (2.15) is known as the continuity equation and states the conservation of mass for the interaction. Furthermore, equation (2.16) describes how the fluid momentum evolves in time and (2.17) is the electrostatic formulation of Gauss' law (2.5). With the fluid equations being coupled to the set of Maxwell's equations they will fully model the laser-plasma dynamics.

2.1.6 Wakefield generation using cold fluid model

When an intense laser pulse impinges a plasma, the electrons will experience a net force which will push them in front of the laser and to its sides [20]. Since the ions are much heavier than electrons, a charge separation is induced by the displaced electrons and stationary ions, resulting in plasma oscillations trailing the pulse. These are known as wakefield oscillations and can be linear or non-linear depending on the intensity of the driving laser pulse.

As a measure of laser intensity, we can consider the normalized peak vector potential given by

$$a_0 = \frac{E_0}{\omega} \tag{2.18}$$

where E_0 is the peak electric field of a laser and ω is the laser frequency. Equation (2.18) describes the peak momentum of electrons attained from an electric field with amplitude E_0 and frequency ω [20]. A laser can be considered relativistically intense if $a_0 \sim 1$ which means that the induced momentum from the field drives the electrons to relativistic velocities which in turn makes interactions non-linear. This means that relativistic effects become important and can be seen in e.g. the second term of equation (2.9) where the velocity of the charged species matter regarding the Lorentz force. Also, approaching relativistic velocities means that the momentum takes on the form $\mathbf{p} = m\mathbf{v}\gamma$. Thus, a velocity close to the speed of light will have a significant impact on $\gamma = \gamma(\mid \mathbf{v} \mid)$ which in turn will impact other quantities in a non-linear way.

In the non-relativistic, linear regime, $a_0 < 1$ and the wakefield oscillations are seen to be purely sinusoidal and travel at a velocity, $v_\phi = v_g$ [20], where v_g is the group velocity of the laser pulse. Furthermore, the electric field created by the charge separation is also periodic. An example of linear plasma waves in one dimension (1D) can be seen in figure 2.1. However, if $a_0 \gtrsim 1$ the interaction can be considered as non-linear and the density perturbations are no longer sinusoidal but rather appear as density spikes. In addition, the space-charge electric field attains a characteristic "sawtooth" shape instead of being sinusoidal. Both these features can be seen in figure 2.1.

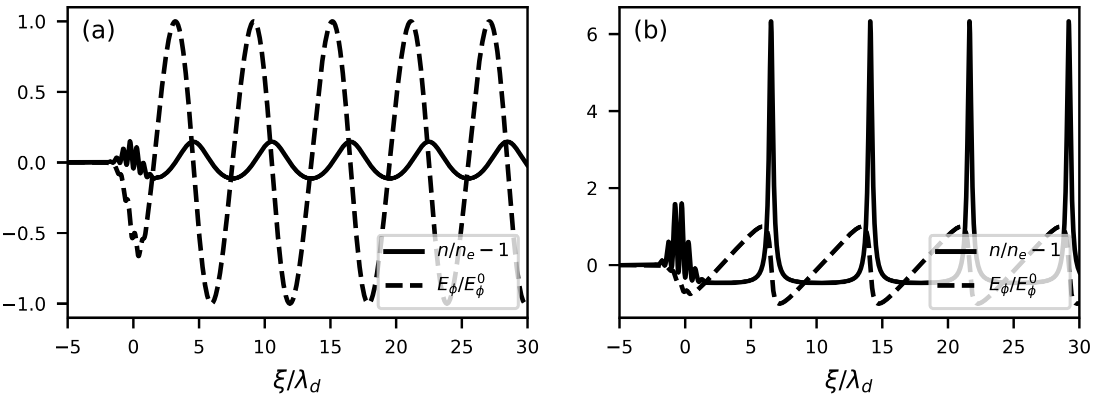

Figure 2.1: Numerical solution of the wakefield model showing the density perturbations (black lines) and electrostatic field (dashed black lines) as functions of the co-moving variable $\xi = x - v_\phi t$ in (a), the linear regime using $a_0 = 0.6$ and (b) the non-linear regime using $a_0 = 2.5$. Both solutions used $v_\phi = 0.961$, $L = \frac{\sqrt{2}}{k_p}$ and $k_d = \frac{\omega_d}{v_\phi}$. Here L is the spatial width of the driver pulse whereas k_d and ω_d are its wavenumber and frequency respectively.

To model the wakefield oscillations, one can exploit the cold fluid model described previously to find numerical solutions for the non-linear interaction in 1D. As a starting point, a useful approximation is to write equations (2.15), (2.16) and (2.17) in 1D with x being the laser propagation direction. Equations (2.15) and (2.17) remain rather unchanged but it is useful to pause and derive the equations of motion for the quantities γ_e and p_x. From the rate of change in four-momentum it is found that [21]

$$\frac{dE_e}{dt} = \frac{d\gamma_e}{dt} = \mathbf{F}_{lorentz} \cdot \mathbf{u} = -\mathbf{E} \cdot \mathbf{u} \tag{2.19}$$

where E_e denotes the electron fluid energy which is directly proportional to γ_e and $\mathbf{u}$ is again the electron fluid velocity. Expressing the longitudinal and transverse electric field in terms of its electrostatic potential as well as vector potential and expressing the transverse fluid velocity in terms of its momentum one can put:

$$\mathbf{E} = -\left(\frac{\partial \phi}{\partial x}, \frac{\partial \mathbf{A}_\perp}{\partial t}\right), \quad \mathbf{u} = \left(u_x, \frac{-\mathbf{A}_\perp}{\gamma_e}\right) \tag{2.20}$$

where in the expression for the transverse component of $\mathbf{u}$, the conservation of transverse canonical momentum, $\mathbf{p}_\perp = q_e \mathbf{A}_\perp$ has been used. This relation will be explained in detail under section 2.3.3. Moving on, the scalar product in equation (2.19) now reads

$$\frac{d\gamma_e}{dt} = u_x \frac{\partial \phi}{\partial x} + \frac{1}{\gamma_e} \mathbf{A}_\perp \cdot \frac{\partial \mathbf{A}_\perp}{\partial t} = u_x \frac{\partial \phi}{\partial x} + \frac{1}{2\gamma_e} \frac{\partial \mathbf{A}_\perp^2}{\partial t}. \tag{2.21}$$

On the other hand, the longitudinal component in equation (2.16) can be used in conjunction with equation (2.21) to yield the evolution of u_x. To begin with, the left hand side can be written

$$\frac{d}{dt}(p_x) = \frac{d}{dt}(\gamma_e u_x) = u_x \frac{d\gamma_e}{dt} + \gamma_e \frac{du_x}{dt} \tag{2.22}$$

where the chain rule has been used. Using the same procedure as before, the x-components of the right hand side of equation (2.16) reads

$$E_x = -\frac{\partial \phi}{\partial x}, \ [\mathbf{u} \times \mathbf{B}]_x = ... = \mathbf{A}_\perp \cdot \frac{\partial \mathbf{A}_\perp}{\partial x}. \tag{2.23}$$

Moving around terms to isolate $\frac{du_x}{dt}$ it is found that

$$\frac{du_x}{dt} = \frac{1}{\gamma_e} \left(\frac{\partial \phi}{\partial x} - \frac{1}{2} \frac{\partial \mathbf{A}_\perp^2}{\partial x} - u_x \frac{d\gamma_e}{dt} \right). \tag{2.24}$$

Applying equation (2.21) the previous equation instead reads

$$\frac{du_x}{dt} = -\frac{1}{\gamma_e^2} \left[\frac{\partial}{\partial x} + u_x \frac{\partial}{\partial t} \right] \frac{\mathbf{A}_\perp^2}{2} + \frac{(1-u_x^2)}{\gamma_e} \frac{\partial \phi}{\partial x}. \tag{2.25}$$

Finally, abbreviating $\mathbf{A}_\perp^2 = a^2$ the full set of cold fluid equations are:

$$\frac{\partial^2 \phi}{\partial x^2} = k_p^2 \left[n_e/n_0 - 1 \right], \tag{2.26}$$

$$\frac{\partial n_e}{\partial t} + \frac{\partial}{\partial x} \left(n_e u_x \right) = 0, \tag{2.27}$$

$$\frac{du_x}{dt} = -\frac{1}{\gamma_e^2} \left[\frac{\partial}{\partial x} + u_x \frac{\partial}{\partial t} \right] \frac{a^2}{2} + \frac{(1 - u_x^2)}{\gamma_e} \frac{\partial \phi}{\partial x}, \tag{2.28}$$

$$\frac{d\gamma_e}{dt} = u_x \frac{\partial \phi}{\partial x} + \frac{1}{2\gamma_e} \frac{\partial a^2}{\partial t}. \tag{2.29}$$

In order to discuss wakefield formation in a simple fashion [22] it is necessary to perform an algebraic transformation from the laboratory frame to a moving frame where the traveling density perturbations are stationary. Such a transformation implies that the independent variables $[x, t] \longrightarrow [\xi, \tau]$ where $\xi = x - v_\phi t$ and $\tau = t$. As a consequence, also the spatial and temporal derivatives transform according to

$$\frac{\partial}{\partial x} \longrightarrow \frac{\partial}{\partial \xi}, \quad \frac{\partial}{\partial t} \longrightarrow \frac{\partial}{\partial \tau} - v_\phi \frac{\partial}{\partial \xi}. \tag{2.30}$$

With this in hand it is possible to rewrite (2.26)-(2.29) as [25]

$$\frac{\partial^2 \phi}{\partial \xi^2} = k_p^2 \left[n_e/n_0 - 1 \right], \tag{2.31}$$

$$\frac{\partial}{\partial \xi} \left(n_e [v_\phi - u_x] \right) = \frac{\partial n_e}{\partial \tau}, \tag{2.32}$$

$$\frac{\partial}{\partial \xi} \left(\gamma_e [1 - v_\phi u_x] - \phi \right) = -\frac{\partial}{\partial \tau} \left(\gamma_e u_x \right). \tag{2.33}$$

To progress, the set of equations (2.31)-(2.33) can be simplified even further. This is done by applying the quasistatic approximation [23]. In other words, in the speed of light frame ($v_\phi = v_g = 1$) the laser pulse is more or less stationary and the plasma is now flowing into it [24]. If in addition the laser field is short enough, the pulse itself and the electrostatic potential driving the wakefield oscillations are assumed to change little during the transit time of the laser pulse through the plasma and a quasistatic state exists [25]. This implies also that the fluid quantities n_e, u_x and γ_e also are in the quasistatic state. Virtually, it means that all fields and quantities are functions of ξ alone and the Poisson equation is seen to take on the form [23]

$$\frac{\partial^2 \phi}{\partial \xi^2} = (k_p \gamma_\phi)^2 \left\{ v_\phi \left[1 - \frac{(1 + a^2)}{\gamma_\phi^2 (1 + \phi)^2} \right]^{-1/2} - 1 \right\} \tag{2.34}$$

where $\gamma_\phi = (1 - v_\phi^2)^{-1/2}$. Once the solution from equation (2.34) is extracted, one can then evaluate all of the fluid quantities as [23]

$$n_e/n_0 = \gamma_\phi^2 v_\phi \left[\left(1 - \frac{(1+a^2)}{\gamma_\phi^2 (1+\phi)^2} \right)^{-1/2} - v_\phi \right], \tag{2.35}$$

$$p_x = \gamma_\phi^2 (1+\phi) \left[v_\phi - \left(1 - \frac{(1+a^2)}{\gamma_\phi^2 (1+\phi)^2} \right)^{1/2} \right], \tag{2.36}$$

$$\gamma = \gamma_\phi^2 (1+\phi) \left[1 - v_\phi \left(1 - \frac{(1+a^2)}{\gamma_\phi^2 (1+\phi)^2} \right)^{1/2} \right]. \tag{2.37}$$

Equations (2.35)-(2.37) are fully non-linear and encapsulate the wakefield generation. In fact, figure 2.1 was generated by solving equation (2.34) numerically and then using the solution for ϕ to compute the remaining fluid quantities.

2.2 Particle-in-cell approach

A well-established method for simulating the interaction of plasma and electromagnetic fields is through a particle-in-cell (PIC) scheme. There are several PIC codes available for download online such as EPOCH [26] and SMILEI [27] but in this thesis SMILEI will be used. In this section the general approach of simulating laser-plasma interactions via the SMILEI PIC scheme will be described. Other PIC codes may differ in terms of code structure and numerical modules but the general method is the same. SMILEI is written in C++ and is developed to run simulations in 1D,2D or 3D on either personal computers or on supercomputer architectures. SMILEI also has a Python interface, allowing the user to launch a simulation using a simple Python script. Post-processing data is also handled through various tools in Python. A brief explanation on how the code simulates laser-plasma phenomena will be given below.

2.2.1 PIC distribution function and quasi-particles

A PIC code simulates plasmas using so called *quasi-particles*, which represent a large number of real particles combined since it is impossible to simulate all charged species within a real plasma. A quasi-particle composed of several electrons will have the same charge to mass ratio as a single electron. This means that both entities are accelerated equally by the Lorentz force. Quasi-particles are used to model the distribution function f_i which is used to describe the plasma as was discussed in section 2.1.4. In SMILEI the simulation is discretized onto a grid of cells where e.g. the electromagnetic fields and the currents are evaluated. In addition the distribution function is discretized as a sum including all of the quasi-particles present within the simulation [27]

$$f_i(\mathbf{r}, \mathbf{p}, t) = \sum_{p=1}^{N_i} M_p \; S(\mathbf{r} - \mathbf{r}_p(t)) \delta(\mathbf{p} - \mathbf{p}_p(t)) \tag{2.38}$$

where N_i is the total number of particles of species i, $\mathbf{r}_p$ the position of the quasi-particle, $\mathbf{p}_p$ the momentum of a quasi-particle, S is the shape function for the particles, δ is the Dirac distribution and M_p is the *weight* of a quasi-particle defined as

$$M_p = \frac{\text{density of species} \cdot \text{hypervolume of cell}}{\text{number of quasi} - \text{particles within the cell}}. \tag{2.39}$$

Note that the units of M_p can vary depending on if the simulation is carried out in 1D,2D or 3D. As an example, if the simulation grid is in 2D the units of M_p is $n_r L_r^2$ (see units of table 2.1). Moving on, it can be shown [27] that the relativistic equations of motion for the quasi-particles can be obtained by first using the expression for f_i in equation (2.38) and putting it into Vlasov's equation (2.12). Then, this result should be integrated over all momenta $\mathbf{p}$ as well as the volume of quasi-particles to yield the final equations of motion

$$\frac{d\mathbf{r}_p}{dt} = \frac{\mathbf{u}_p}{\gamma_p} \tag{2.40}$$

$$\frac{d\mathbf{u}_p}{dt} = \frac{q_i}{m_i}(\mathbf{E}_p + \frac{\mathbf{u}_p}{\gamma_p} \times \mathbf{B}_p) \tag{2.41}$$

where the reduced momentum has been introduced as $\mathbf{u}_p = \frac{\mathbf{p}_p}{m_i}$ and again the Lorentz factor is $\gamma_p = \sqrt{1 + \mathbf{u}_p^2}$. This allows the PIC code to integrate the equations of quasiparticles as if they were real particles subject to the Lorentz force.

2.2.2 Maxwell's equation on the Yee grid

To solve Maxwell's curl equations (equation (2.8) and (2.6)) one makes use of the finite difference time domain (FDTD) method [28]. This means that both space and time are discretized into equidistant points on a special space-time grid which is also known as a Yee grid. For instance, in 1D it would be possible to divide a simulation of spatial length X and temporal length T into finite points $N_{x,t}$ with distance $\Delta_{x,t}$ as $X = N_x \Delta x$ and $T = N_t \Delta t$ respectively. Differential operators acting on the fields are then replaced with Taylor approximations around these distinct space-time points. To illustrate this, consider the 1D example where any function f of a single variable x is Taylor expanded around $\pm\Delta x$ up to order $\mathcal{O}(\Delta x^2)$. These expressions can be combined to form

$$\frac{\partial f}{\partial x} = \frac{f(x + \Delta x/2) - f(x - \Delta x/2)}{\Delta x} + \mathcal{O}(\Delta x^2) \tag{2.42}$$

which is useful whenever expressions for the fields such as $\frac{\partial B}{\partial t}$ or $\frac{\partial E}{\partial x}$ appears in the Maxwell curl equations. Please note that this choice of discretization introduces a shift of $\Delta t/2$ and $\Delta x/2$ in B_y and E_z respectively which defines the staggered Yee grid. The reason for this is that the Yee grid provides a robust way to approximate Maxwell's equations which ensures that phyiscal boundary conditions are fulfilled [28]. In addition to this, equation (2.42) is also "second-order accurate" which means that the error term, $\mathcal{O}(\Delta x^2)$ approaches zero as the square of the grid step.

2.2.3 SMILEI simulation loop

With the relevant tools and equations at hand it is time to explain how SMILEI generates output given input parameters.

The SMILEI code is initialized by loading the charged quasi-particles into the simulation domain (if any are prescribed by the user) which are then used to calculate the total charge and current densities in accordance with equation (2.13) and (2.14). Note that the user also has to specify how the particles are oriented in the grid and what momentum initialization they will have. Then the Poisson equation is solved to yield the initial electrostatic fields. Lastly the code begins to repeat a number of steps for the N_t timesteps assigned to the simulation which will advance it in time. These steps are as follows:

- Electromagnetic fields are first interpolated at the quasi-particles positions.
- Positions and velocities for the particles are computed using a so called *leap-frog* scheme [27] which utilizes equations (2.40) and (2.41) on the staggered grid.
- The new charge and current densities are projected into the simulation grid.
- The corresponding new electromagnetic fields are now computed on the grid.

After N_t timesteps the simulation is completed and the output can be post-processed by the user. This is a very brief overview on how the SMILEI code works and the interested reader may find a detailed explanation in [27].

2.3 Plasma wakes and sub-cycle pulse generation mechanism

It is possible to amplify a long-wavelength laser by having it interact with moving electron plasma wakes generated by an intense driving laser pulse. This is referred to as laser wakefield driven amplification (LWDA) and will be reviewed below. In addition to this, the relevant theoretical framework to describe LWDA will be presented as well.

2.3.1 Laser wakefield driven amplification

One mean of generating sub-cycle laser pulses is through the scheme of laser wakefield driven amplification [15]. This is done by letting a relativistically intense ($a_0 > 1$) laser pulse propagate through a plasma and induce wakefield oscillations. As was stressed earlier, with such intense lasers, the laser-plasma interaction is non-linear which implies that the density perturbations are pronounced and virtually Gaussian in nature. Then, a sub-relativistic ($a_0 \ll 1$) seed laser pulse with much longer wavelength is injected along with the driving laser field. This seed field has orthogonal polarization to the driver. As the seed pulse is traveling inside the plasma it interacts with the electron plasma wake induced by the driver pulse. Each density perturbation can modulate the seed, increasing its amplitude as well as up-shifting its frequency. However, only the first and most prominent density spike will increase the laser pulse amplitude significantly meaning that highly intense, isolated pulses are produced. In [15], 2D and 3D PIC simulations on LWDA were carried out which yielded sub-cycle fields with amplitudes almost 20 times larger than the initial seed laser as can be seen in figure 2.2(b). Moreover, this method allows to tune the carrier envelope phase (CEP) using the seed pulse CEP or driver delay which is demonstrated in figure 2.2(c). Frequency tunability can be achieved by changing the driving laser and plasma parameters and is depicted in figure 2.3.

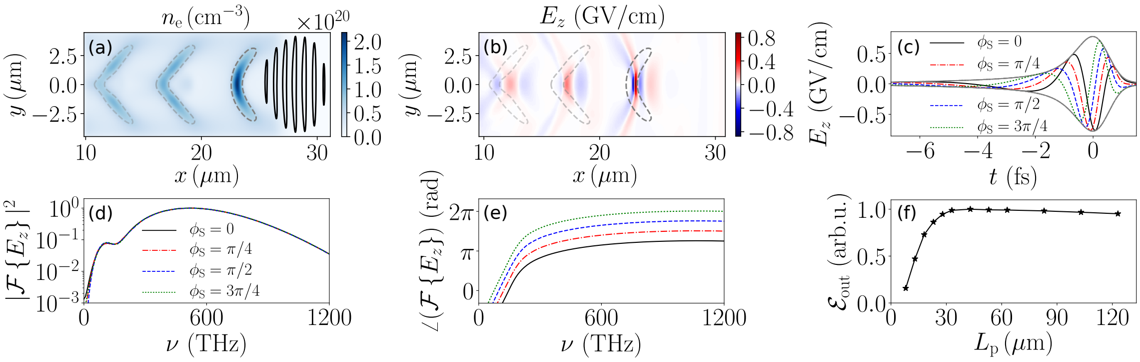

Figure 2.2: 2D SMILEI PIC simulations using a seed pulse with electric field amplitude $E_s^0 = 0.04$ GV/cm. In (a) electron density contours with $n_e(x, y) = \max(n_e)/3$ is shown (dashed lines) whereas the electric field contours are shown with $E_y(x, y) = \max(E_y)/4$ (solid lines), (b) shows the amplified electric field E_z along with electron density contours, (c) depicts the on-axis electric field E_z for different CEP of the seed under their common envelope (gray), (d) and (e) are the corresponding power spectrum and spectral phase and (f) shows the plasma length L_p dependency on the sub-cycle pulse energy. Reprinted from [15].

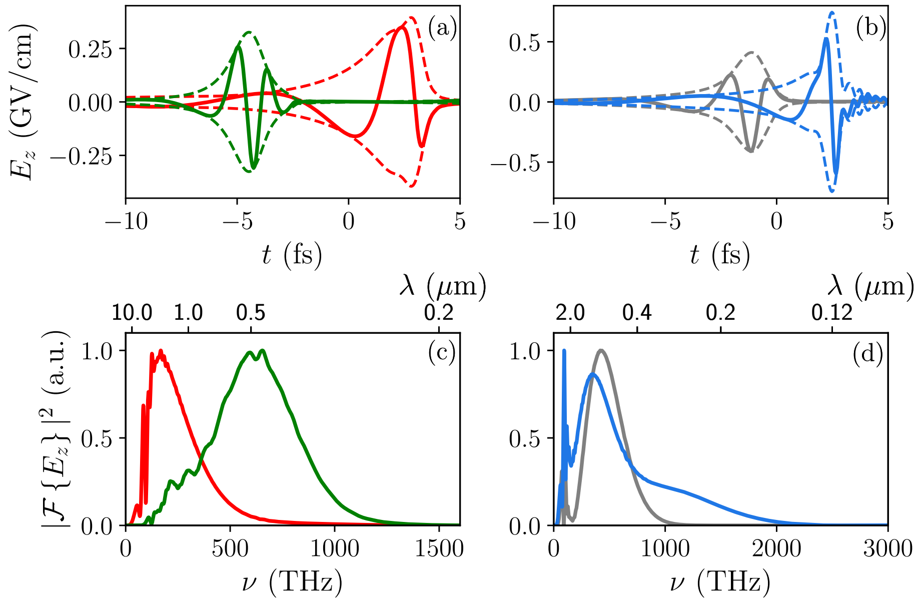

Figure 2.3: On-axis electric field E_z for the sub-cycle field (top panel) is shown together with its corresponding power spectrum (bottom panel). In (a,c) the spectral tunability is demonstrated by altering the electron density whereas in (b,d) spectral tunability is induced by changing the driving electric field amplitude E_d^0. Reprinted from [15].

2.3.2 Energy gain in LWDA

It is possible to use the framework of the cold fluid description in order to qualitatively understand why amplification occurs. It can be shown that laser fields can be amplified by the n_e/γ_e distributions to gain energy (in 1D) [5], [15]

$$U_{gain}(t) = \frac{1}{2}\int_{-\infty}^{t} A_z^2 \frac{\partial}{\partial \tau}\left(\frac{n_e}{\gamma_e}\right) d\tau \tag{2.43}$$

where A_z is the transverse vector potential of the field. From this it is a simple matter to see that whenever the electron plasma n_e/γ_e profile is increasing in time, there is also an energy gain to the field. On the contrary, if the profile is descending, a net loss of energy is present. Another important feature of equation (2.43) is that the existence of A_z^2 determines whether energy can be gained, i.e. if amplification is possible. If A_z is rapidly oscillating, as is the case of a short wavelength laser, then loss and gain can compensate each other. This implies that in order to have amplification, the wavelength of the seed laser needs to be greater than the dimensions of the electron density spike. While this provides qualitative picture of the interaction, it is the purpose of this thesis to go beyond this theory and gain a quantitative understanding.

2.3.3 Evolution equation for the transverse vector potential in 1D

Dynamics of the cold fluid model also allows one to derive the evolution equation for the transverse electromagnetic vector potential in the framework of LWDA. To derive this, it will be useful to first examine the transverse components of equation (2.16) in 1D along x ($\frac{\partial}{\partial y} = \frac{\partial}{\partial z} = 0$) :

$$\left(\frac{\partial}{\partial t} + u_x \frac{\partial}{\partial x}\right) p_y = q_e(E_y - u_x B_z) \tag{2.44}$$

$$\left(\frac{\partial}{\partial t} + u_x \frac{\partial}{\partial x}\right) p_z = q_e(E_z + u_x B_y) \tag{2.45}$$

where u_x is the longitudinal component of the electron fluid velocity and q_e is again the electron charge. By introducing the electromagnetic vector potential $\mathbf{A} = \mathbf{A}(\mathbf{r}, t)$ and exploiting the freedom of using the Coulomb gauge ($\nabla \cdot \mathbf{A} = 0$) the electromagnetic fields are written

$$\mathbf{E} = -\frac{\partial \mathbf{A}}{\partial t},\ \mathbf{B} = \nabla \times \mathbf{A}. \tag{2.46}$$

Now equations (2.44) and (2.45) can be cast in the following form

$$\frac{\partial}{\partial t}\left(p_y + q_e A_y\right) = -u_x \frac{\partial}{\partial x}\left(p_y + q_e A_y\right) \tag{2.47}$$

$$\frac{\partial}{\partial t}\left(p_z + q_e A_z\right) = -u_x \frac{\partial}{\partial x}\left(p_z + q_e A_z\right) \tag{2.48}$$

where A_y and A_z are the transverse components of $\mathbf{A}$. In the far past, before any interaction with the laser pulse takes place ($t \longrightarrow -\infty$) [5]

$$p_y + q_e A_y = 0 \tag{2.49}$$

$$p_z + q_e A_z = 0 \tag{2.50}$$

everywhere in the spatial interaction region. This means that equations (2.47) and (2.48) indicate that the transverse fluid momentum evolves as (writing in terms of the electric field)

$$\frac{\partial \mathbf{p}_\perp}{\partial t} = q_e \mathbf{E}_\perp \tag{2.51}$$

which is also the statement of conservation of transverse canonical momentum

$$\mathbf{p}_\perp = -q_e \mathbf{A}_\perp. \tag{2.52}$$

Equation (2.51) is coupled to the set of Maxwell's equations in order to describe the laser-plasma dynamics and will be of importance later when discussing the numerical approach of LWDA. However, working with equation (2.52) it is possible to attain the wave equation for the transverse components of $\mathbf{A}$. To begin with, stating the Maxwell-Ampère law for the vector potential in Coulomb gauge gives

$$-\nabla^2 \mathbf{A} = \mathbf{J} - \frac{\partial^2 \mathbf{A}}{\partial t^2} \tag{2.53}$$

where $\mathbf{J}$ is the current density. Rearranging and examining only the z-component of equation (2.53) it now reads

$$(\frac{\partial^2}{\partial t^2} - \frac{\partial^2}{\partial x^2}) A_z(x,t) = J_z. \tag{2.54}$$

In this framework, the transverse current density, J_z will be given as

$$J_z = \rho_e v_z = (n_e q_e) \cdot \frac{p_z}{\gamma_e} = -\frac{n_e}{\gamma_e} p_z \tag{2.55}$$

where $\rho_e = n_e q_e = -n_e$ is the electron charge density, n_e is the electron number density and γ_e is the Lorentz factor of the moving electron fluid. Again p_z is the transverse momentum of the electron fluid. In the last step of equation (2.55), $q_e = -1$ has been used. Before moving on, it will be assumed that γ_e remains constant throughout the interaction but allow n_e to be a function of x and t. To progress, the expression of equation (2.55) can be used in conjunction with the conservation of transverse canonical momentum which will turn equation (2.54) into the following form

$$(\frac{\partial^2}{\partial t^2} - \frac{\partial^2}{\partial x^2}) A_z(x,t) + \frac{n_e}{\gamma_e} A_z(x,t) = 0. \tag{2.56}$$

This is the evolution equation for the electromagnetic interaction for the transverse vector potential A_z. This can be solved numerically but in this thesis the analytical solution will be examined as well. Take note of the appearance of n_e/γ_e in equation (2.56) which implies that refraction does not depend on the electron density alone and is true for non-stationary plasmas in this framework. Refraction is what in turn governs signal transparency.

3

Methods

This chapter will be divided into two major sections with section 3.1 focusing on the analytical approach of LWDA, briefly introducing the method of Green's functions and then giving the derivation of the outgoing field using equation (2.56). Then, section 3.2 will cover the numerical implementation of LWDA using the SMILEI PIC code. Moreover, a custom code utilizing the technique of FDTD combined with the non-linear wakefield model from section 2.1.6 is proposed and benchmarked.

3.1 Analytical approach

For the theoretical analysis, this section begins by introducing the method of Green's functions in order to solve partial differential equations in the framework of LWDA. This framework is applied to equation (2.56) in order to attain the solution for the transverse vector potential A_z which in turn is related to the transverse field E_z. Once the expression for E_z is extracted it is possible to inspect how the frequency and amplitude of the field has changed.

3.1.1 Method of Green's functions

A versatile way of solving inhomogeneous partial differential equations is by utilizing Green's functions. Consider the following example PDE in two dimensions

$$\mathcal{L}f(x,y) = S(x,y) \tag{3.1}$$

where $\mathcal{L}$ is any linear differential operator, $f(x,y)$ is the solution and $S(x,y)$ is any function depending on the variables x and y. To solve equation (3.1) by general means can be quite tedious since $S(x,y)$ is not a constant. A method making use of so called Green's functions can be a viable alternative to solve equation (3.1). For this example, such a function would satisfy

$$\mathcal{L}G(x,x',y,y') = \delta(x-x')\delta(y-y') \tag{3.2}$$

where $G(x,x',y,y')$ is the Green's function and $\delta(x)$ is the Dirac delta distribution. By solving (3.2) one can obtain G subject to some boundary conditions. A Green's function depends on what kind of linear operator one has and also what the boundary conditions are. Once G is known, the solution to equation (3.1) is obtained by integrating G together with S over the domain in question, σ

$$f(x,y) = \int\int_{\sigma} G(x,x',y,y')S(x',y')dx'dy'. \tag{3.3}$$

To show that this is a solution, apply the linear differential operator to equation (3.3) and then make use of equation (3.2) :

$$\mathcal{L}f(x,y) = \int\int_{\sigma} \mathcal{L}G(x,x',y,y')S(x',y')dx'dy' = \tag{3.4}$$

$$\int\int_{\sigma} \delta(x-x')\delta(y-y')S(x',y')dx'dy' = S(x,y).$$

In the last line of equation (3.4) the integral property of the Dirac distribution was employed, namely

$$\int_C f(x)\delta(x-b)dx = f(b) \tag{3.5}$$

which holds as long as $b \in C$. This result can of course be generalized to any dimension of the problem. In this thesis and especially in the study of waves, f would be the wave solutions generated by a localized source distribution S. Then one can describe the Green's equation (3.2) as a simple wave equation generated by a strongly localized unit source. Thus, adding (integrating) the unit contributions over the distributed source S with G is seen to solve the wave equation.

3.1.2 Application of Green's function to wave equation

It is now time to apply the method of Green's functions in order to solve equation (2.56). This will be studied under the assumption that the electron plasma wake is interacting with a continuous wave (CW) seed laser. Then it will be of interest to see if this can describe how the frequency and amplitude of the incoming wave is altered.

As a starting point, the second term of equation (2.56) is moved to the right-hand side which will be interpreted as our source that will produce solutions for A_z (see equation (3.1)). From the discussion of Green's functions above it is possible to write the solution for A_z (equation (3.3)) as

$$A_z(x,t) = \frac{1}{\gamma_e}\int_{-\infty}^{\infty}\int_{-\infty}^{\infty} G(x,x',t,t')n_e(x',t')A_z(x',t')dt'dx' \tag{3.6}$$

where $G(x,x',t,t')$ is the Green's function corresponding to the interaction setup. Integration needs to be over all space and all times in order to add up all of the source. Note that it was clarified in section 2.3.3 that γ_e is allowed to be considered constant whereas now n_e should be a function of space and time. Moving on, G has to be specified for the calculation to continue. Such a function depends on the linear operator $\mathcal{L}$ of the problem as well as the boundary conditions. A similar approach has been done in [9] where a Green's function of the form

$$G(x,x',t,t') = \frac{1}{2}\Theta\left[t-t'- \mid x-x' \mid\right] \tag{3.7}$$

is used and Θ is the Heaviside step function. To support this choice of Green's function further, in [29] the same expression is attained for the linear operator appearing in wave equation (2.56). Since there is a term of $\mid x - x' \mid$ within our Green function, it is possible to write it as

$$G(x, x', t, t') = \begin{cases} \frac{1}{2}\Theta\left[t - t' - (x - x')\right] & x > x' \\ \frac{1}{2}\Theta\left[t - t' + (x - x')\right] & x < x' \end{cases}$$

and the form of G should be chosen so that $x > x'$ which should be interpreted as waves traveling to the right of the source. In what follows, the source is the traveling electron plasma wake which is taken to have a non-evolving shape. Therefore, it is assumed that no waves are reflected and only the incident wave is modulated and keeps propagating to the right. With this Green function we write the solution for A_z as

$$A_z(x, t) = \frac{1}{2\gamma_e} \int_{-\infty}^{\infty} \int_{-\infty}^{\infty} \Theta\left[t - t' - x + x'\right] n_e(x', t') A_z(x', t') dt' dx'. \tag{3.8}$$

In order to make progress, it is possible to employ a trick also used in [9] which is to work with the electric field, $E_z = -\frac{\partial A_z}{\partial t}$. Then, by applying $-\frac{\partial}{\partial t}$ to equation (3.8) one ends up with the electric field on the left-hand side whereas the Heaviside step function inside the integral becomes

$$\frac{\partial}{\partial t}\Theta\left[t - t' - x + x'\right] = \delta\left(t - t' - x + x'\right). \tag{3.9}$$

This is very convenient because there is an option to eliminate one of the integration variables by using the Dirac delta distribution property of equation (3.5). Employing this when integrating with respect to t' the solution is now written

$$E_z(x, t) = \frac{-1}{2\gamma_e} \int_{-\infty}^{\infty} n_e(x', t - x + x') A_z(x', t - x + x') dx' \tag{3.10}$$

where the function n_e and the solution A_z are now evaluated at $t' = t - x + x'$. Equation (3.10) is an integral equation [1] and there are numerous yet limited analytical techniques to solve them [30]. To find a closed form of the expression for $E_z(x, t)$, an assumption will be made on the solution, A_z appearing under the integral sign in equation (3.10). It can be approximated by the incoming CW seed laser. This means that the electron plasma wake is affected only by the seed laser and is not self-consistently modulated by any produced fields. This approximation allows one to replace the expression for A_z under the integral sign by

$$A_z(x, t) \longrightarrow A_s(x, t) = a_s^0 e^{i(k_s x - \omega_s t)} \tag{3.11}$$

where a_s^0 is the dimensionless amplitude, k_s is the wavenumber and ω_s is the frequency of the CW seed laser. Here the complex representation is used due to its mathematical versatility and it is understood that one will take the real part of the final result. In addition to this, the electron density is specified as

$$n_e(x, t) = n_e^{max} e^{-\frac{(x - v_\phi t)^2}{v_\phi^2 t_e^2}} \tag{3.12}$$

---

[1] For the interested reader this is properly referred to as a homogeneous Fredholm integral equation of the second kind.

where n_e^{max} is the peak density of the density perturbation, v_ϕ is the corresponding phase velocity and t_e its duration.

By putting in the expressions of (3.11) and (3.12) into equation (3.10) and making some simplifications it is found that

$$E_z(x,t) = \frac{-n_e^{max} a_s^0}{2\gamma_e} e^{i\omega_s(x-t)} e^{-\frac{(t-x)^2}{t_e^2}} \int_{-\infty}^{\infty} e^{-\frac{x'^2\widetilde{v}^{-2}}{t_e^2}} e^{\left(i(k_s-\omega_s)-\frac{2(t-x)\widetilde{v}^{-1}}{t_e^2}\right)x'} dx' \tag{3.13}$$

where $\widetilde{v}^{-1} = 1 - 1/v_\phi$ has been introduced. Note that all independent terms have been taken outside the integral in equation (3.13) and that the remainder of terms appearing under the integral sign can be converted into a standard Gaussian integral by completing the square in the exponents. This calculation is omitted and the final result is simply stated as

$$E_z(x,t) = \frac{-n_e^{max} a_s^0 t_e \sqrt{\pi}}{2\gamma_e \widetilde{v}^{-1}} \cdot e^{i(\omega_s + \frac{k_s-\omega_s}{\widetilde{v}^{-1}})(x-t)} \cdot e^{-\frac{(k_s-\omega_s)^2}{4\widetilde{v}^{-2}}} . \tag{3.14}$$

Looking at equation (3.14) one will see that the wave solution is again in the CW mode and not a laser pulse. The reason is because in the latter, the field expression should contain an oscillatory component multiplied with a Gaussian envelope. Moreover the oscillating part of equation (3.14) appears to be frequency shifted by a term $\frac{k_s-\omega_s}{\widetilde{v}^{-1}}$ along with the amplitude of the wave being different due to the prefactor and the exponential term. Thus, it appears that the initial seed laser has a new frequency and amplitude which is the desired property to describe LWDA. However, a dispersion relation for $k_s = k_s(\omega_s)$ is needed to make predictions regarding the frequency and amplitude alterations. Since the interaction takes place within a plasma containing wakefield oscillations there is no linear dispersion relation available and it will prove difficult to make physical results of equation (3.14). This will be discussed more in detail later.

3.2 Numerical approach

In order to compare and justify the 1D theory outlined above, numerical investigations of LWDA have been performed in 1D. To add further, 2D and 3D PIC simulation results have already been introduced in section 2.3.1 and could also be used to analyze said theory.

This section begins by explaining how the 1D SMILEI PIC simulations were initialized in the framework of LWDA. Then, the approach of building an independent code solving Maxwell's equations in 1D using the method of FDTD in conjunction with the non-linear wakefield model is presented. This code can be viewed and downloaded at `https://github.com/Chriolo/FDTD_Wakefields`.

3.2.1 PIC approach to LWDA in 1D

A brief explanation of how the SMILEI code works has been provided in section 2.2 and here it will be described how the simulations were initialized in order to yield the results of a 1D LWDA setup.

As a start, it is crucial to choose a reference frequency of the problem and that other quantities will have its units normalized in terms of this frequency (see table 2.1). For this thesis the frequency of the driving laser pulse, ω_d is chosen as a reference so that $\omega_r = \omega_d$. This means that e.g. all spatial lengths are measured in terms of the driver wavelength, λ_d as $L_r = 2\pi c/\omega_d = \lambda_d$ and all temporal durations in optical-cycles of the pulse. To clarify this, one optical-cycle of the driving pulse amounts to the reference time, $T_r = 2\pi/\omega_d$ which is the inverse of its frequency.

This simulation has a duration of $250 \cdot T_r$ and uses a spatial grid with a total length of $64\lambda_d$ and a plasma extending up to $37.5\lambda_d$. This plasma slab has a linear density ramp up and ramp down to and from $0.026n_r$ over the length of one driver wavelength so in total the plasma slab occupies $39.5\lambda_d$ of the spatial grid. Moreover the plasma is composed of two species, ions and electrons where the ions are immobile and only act as a neutralizing background. Furthermore, all quasi-particles constituting this plasma are initialized with a random spatial position within the slab profile and their initial momentum are set so that they have momentum corresponding to zero temperature. This simulation uses 1000 quasi-particles per cell.

Regarding electromagnetic fields, a pump laser pulse which will excite the plasma wake is launched from the leftmost part of the simulation grid along with a monochromatic seed laser having orthogonal polarization to it. It is possible to place diagnostic tools inside the simulation grid which can measure a wide variety of output such as electromagnetic fields, densities, energy and so on. Such tools are placed within the grid so that it is possible to extract information on how the seed laser is modulated. All important input quantities are listed in table 3.1. Note that the value used for the FWHM of the driving laser temporal envelope is chosen to be in an efficient regime to generate plasma wakes [23]. More specifically, the driver pulse length has to be smaller than a plasma period.

Results for the sub-cycle pulse generation in this frame will be given later but it is useful to show how SMILEI can describe wake formation using the above setup. In figure 3.1 one can find how the electron number density varies in space along with the driving laser field at one particular timeframe. Indeed the code produces nonlinear wakes with the rightmost one ($x/\lambda_d \sim 25$) being the most prominent having almost an order of magnitude increase as compared to the ambient density.

3.2.2 LWDA using an independent FDTD code

By using SMILEI, the Vlasov-Maxwell equations are solved self-consistently provided input parameters in the form of a Python script given by the user. Another option is by studying and solving equation (2.56) which can be done numerically using the FDTD scheme which is utilized by SMILEI. Actually, to be able to use the method of FDTD its easier to work with the **E** and **B** fields instead of the vector potential **A**. Instead, starting from the transverse components of Maxwell's equations (2.6) and (2.8) in 1D they read

$$\partial_x E_z = \partial_t B_y, \quad \partial_x B_y = \partial_t E_z + J_z \tag{3.15}$$

$$\partial_x E_y = -\partial_t B_z, \quad -\partial_x B_z = \partial_t E_y + J_y. \tag{3.16}$$

From here it is assumed that the plasma is cold so that the cold fluid model can be employed. As a reminder, the electron fluid evolves according to equation (2.51) and has to be coupled with equations (3.16) and (3.15). Since the interaction is identical in the transverse directions it is enough to couple (3.15) with the electron fluid evolution in the code. Finally, by writing $J_z = \frac{n_e}{\gamma_e} p_z$ one arrives at the coupled equations governing the laser-plasma interaction :

$$\partial_t E_z = \partial_x B_y - \frac{n_e}{\gamma_e} p_z \tag{3.17}$$

$$\partial_t B_y = \partial_x E_z \tag{3.18}$$

$$\partial_t p_z = E_z. \tag{3.19}$$

To solve this by the method of FDTD equation (2.42) must be used to approximate the derivatives appearing in this system. In doing so, a shift of $\Delta x/2$ and $\Delta t/2$ in $E_z(x,t)$ and $B_y(x,t)$ is produced as can be seen in equation (2.42). To better illustrate this, consider writing any continuous field, $F = F(x,t)$ onto the grid as described in section 2.2.2 on a discrete space-time point $[x_i, t_k]$ as

$$F(x_i = i\Delta x, t_k = k\Delta t) \equiv F_k^i \tag{3.20}$$

where it is understood that i and k represent at which temporal and spatial step the function is evaluated at and $i, k = 0, 1, 2, 3.., N_{x,t}$ are the spatial and temporal

Input quantity	**Value**
Simulation duration	$250 \cdot T_r$
Simulation grid length	$64 \cdot L_r$
Cell length	$L_r/180$
Time step	$T_r/194$
Plasma flat top length	$37.5 \cdot L_r$
Plasma ramp length	$1 \cdot L_r$
Ambient plasma density	$0.026 \cdot n_r$
Driver laser normalized amplitude	2.5
Driver frequency	$1\omega_r$
FWHM of driver envelope	$3.115 \cdot T_r$
Seed laser normalized amplitude	0.005
Seed laser frequency	$0.2\omega_r$
Particles per cell	1000
Position initialization	"random"
Momentum initialization	"cold"

Table 3.1: Table containing the input quantities used for the simulation and their values.

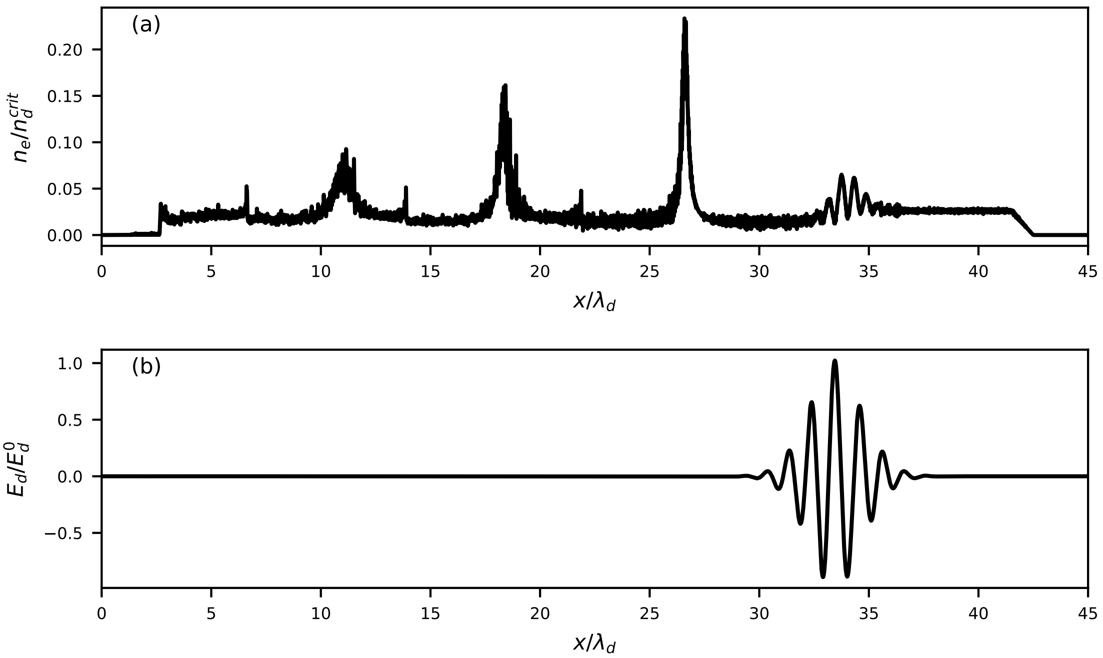

Figure 3.1: PIC simulation demonstrating electron density perturbations driven by a laser pulse with $a_0 = 2.5$. In (a) the electron density modulations is shown whereas in (b) the electric field of the driving laser pulse is depicted. Both frames have been taken at the same timeframe corresponding to $\sim 60\%$ of the simulation time.

indices respectively. Then, as an example consider using equation (2.42) (neglecting the error term) to evaluate the spatial derivative of F so that

$$\frac{\partial F(i\Delta x, k\Delta t)}{\partial x} = \frac{F(i\Delta x + \Delta x/2, k\Delta t) - F(i\Delta x - \Delta x/2, k\Delta t)}{\Delta x} = \frac{F_k^{i+1/2} - F_k^{i-1/2}}{\Delta x} \tag{3.21}$$

which induces a shift of $\Delta x/2$. For the sake of readability, the transverse fields, momentum and electron density are now written as $E_z = E$, $B_y = B$, $p_z = p$ and $n_e = n$. Using the above procedure the set of equations (3.17)-(3.19) are transformed and can be expressed recursively as :

$$E^i_{k+1/2} = E^{i-1}_{k+1/2} + \frac{\Delta t}{\Delta x}(B^{i-1/2}_{k+1} - B^{i-1/2}_{k}) - \frac{\Delta t}{\gamma_e} n^{i+1/2}_{k+1/2} p^{i+1/2}_{k+1/2} \tag{3.22}$$

$$B^{i+1/2}_k = B^{i-1/2}_k + \frac{\Delta t}{\Delta x}(E^i_{k+1/2} - E^i_{k-1/2}) \tag{3.23}$$

$$p^{i+1/2}_{k+1/2} = p^{i-1/2}_{k+1/2} + \Delta t E^i_{k+1/2} \tag{3.24}$$

so that all quantities involving the future temporal and spatial steps can be written in terms of the previous ones. Thus, equation (3.22) gives the new electric field sample at a spatial step i using the previous value at $i-1$ which is taken to be already known plus the rest of the fields evaluated at intermediate steps. Furthermore, these equations have to be solved in the order $E \longrightarrow B \longrightarrow p$ since e.g. the updated value of $B_k^{i+1/2}$ in equation (3.23) requires the value of $E^i_{k+1/2}$ from equation (3.22) and so on. Lastly, as with all FDTD schemes, these must satisfy the

Courant–Friedrichs–Lewy (CFL) condition [28] which is related to the spatial and temporal steps $\Delta_{x,t}$. In 1D the condition states that to ensure numerical stability and avoid exponential growth of the electromagnetic fields, the time step must satisfy: $\Delta t \leq \Delta x$. FDTD simulations in this thesis uses a temporal step $\Delta t \sim 0.875\Delta x$ in order to respect the CFL limit while still maintaining a good temporal resolution.

All of this can be programmed into Python where a user-specified density profile can be used so that the system of updating equations (3.22)-(3.24) can be solved to give output in the form of arrays of field values. Next, some brief benchmarks are given to illustrate how this scheme can describe vacuum propagation of laser fields but also their reflection at overdense plasmas.

3.2.3 Laser pulse propagation and reflection

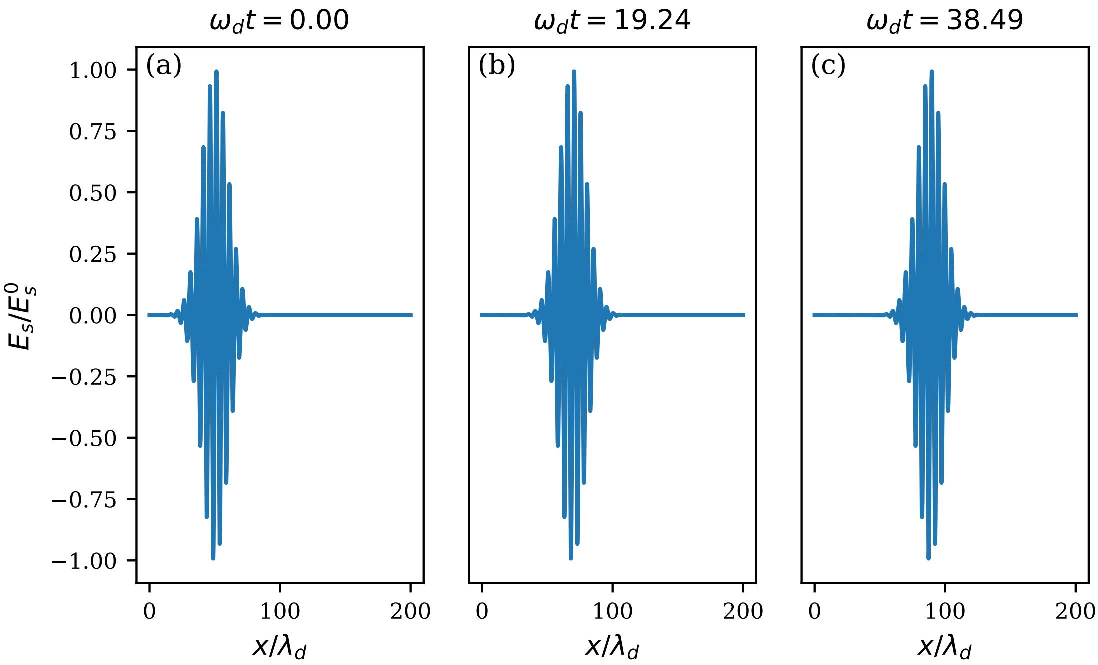

Figure 3.2: FDTD simulation demonstrating the vacuum propagation of the seed electric field in time.

To make sure the code is functioning properly it is useful to see if it will describe basic physical features such as laser propagation in vacuum and reflection at an overdense plasma. For these simulations, a forwards propagating laser pulse with $\omega_s = 0.2\omega_d$ having the initial condition $E_z(t) = E_s^0 \sin(\omega_s t) e^{-t^2/(2t_0)^2}$ where t_0 is the width of the pulse, set to contain few cycles. In figure 3.2 one can see how the laser pulse is properly traveling to the right whereas in figure 3.3 the very same laser is perfectly reflected at the surface of an overdense plasma. In vacuum, the code properly simulates the speed of propagation of the laser pulse in vacuum which was found to be $v_g = 1.000074 \pm 5.5 \cdot 10^{-6}$. For the density of the plasma slab, a number density of $n_e > n_c^d$ along with a width of $20\lambda_d$ is used.

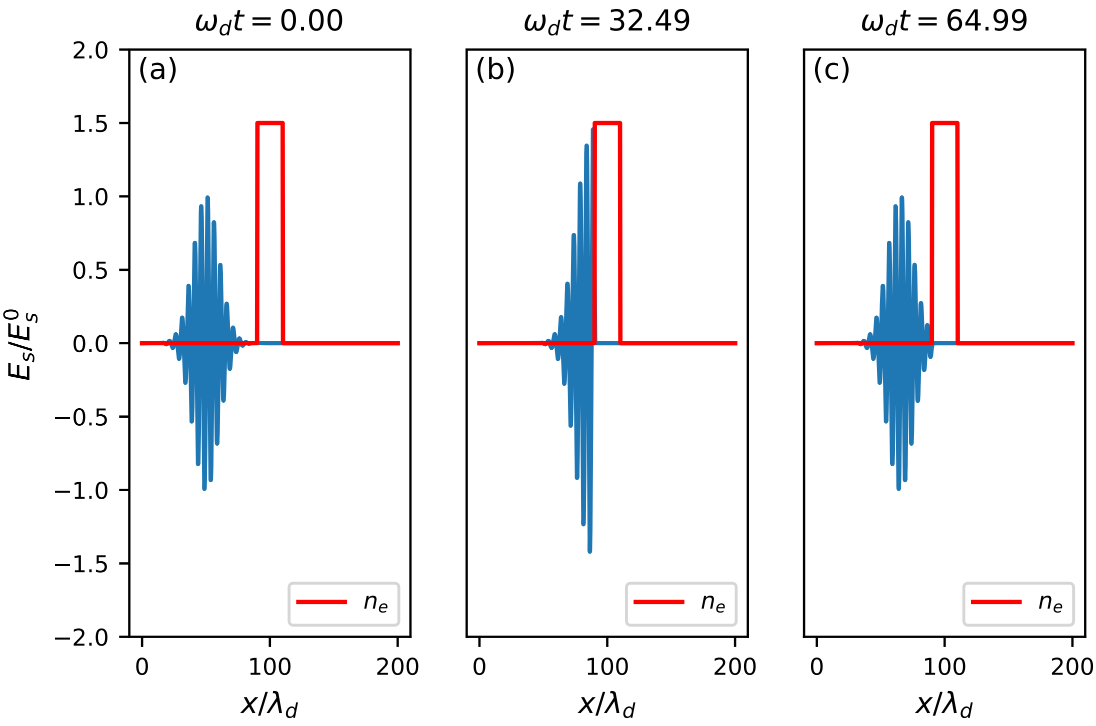

Figure 3.3: FDTD simulation demonstrating the reflection of a seed laser pulse at an overdense plasma.

It is also possible to manipulate a seed laser pulse with an arbitrary n_e/γ_e profile in this scheme. However, for the setup of LWDA, such profiles have to travel at a certain phase velocity and have the correct non-linear structure as given in section 2.3. Theory regarding non-linear wakefield oscillations was also given in section 2.3 and the remaining part is to give a brief explanation how this is imported into the FDTD code.

Equation (2.34) is solved numerically[2] with a basic Python integration tool in the co-moving frame where ξ is the dependent variable. Once this is done, the remaining fluid quantities (equations (2.35)-(2.37)) can then be computed by specifying a driving laser pulse profile a. As previously mentioned, such a profile can be specified as a function of ξ only. To see this, the vector potential of the short, driving laser pulse with frequency ω_d and wavenumber k_d can be expressed as

$$a(x,t) = a_d^0 \sin(k_d x - \omega_d t) \cdot e^{-\frac{(x-v_g t)^2}{L^2}} = a_d^0 \sin(k_d(x - v_p t)) \cdot e^{-\frac{\xi^2}{x_0^2}} \tag{3.25}$$

where L is the spatial width, a_d^0 is the normalized driver amplitude, v_p and v_g are the phase and group velocities of the driver respectively. Further, it is assumed that the pulse is centered at $x = 0$. By adding and subtracting the term $v_g t$ to the argument of the oscillating part of equation (3.25), one can form

$$a(\xi,t) = a_d^0 \sin(k_d(\xi + (v_g - v_p)t)) \cdot e^{-\frac{\xi^2}{L^2}}. \tag{3.26}$$

---

[2] Analytical solutions of this equation can be found by using square laser pulse profiles, see [31] and [32].

Note that $v_g \sim v_p \sim 1$ which implies that the additional term $(v_g - v_p)$ can be neglected. Finally, this leads to the desired expression for the pulse profile

$$a(\xi) = a_d^0 \sin(k_d \xi) e^{-\xi^2/L^2}. \tag{3.27}$$

Having both the density and γ_e profile for the non-linear interaction it is possible to interpolate the total n_e/γ_e profile onto the simulation grid given by the FDTD code. It is interpolated in such a way that the total profile is given by each value of $x - v_g t$ so that it is co-moving with the seed laser pulse to the right. With this in hand one is very close to the SMILEI simulation setup of LWDA as one can now simulate how Maxwell's equations behave when there is a source term given by the non-linear plasma wake model.

Results following from the wakefield model will use the following input parameters: $a_d^0 = 2.5$, $v_\phi = v_g = 0.987$ $k_d = \omega_d/v_p = 1/0.987$, $n_0 = 0.026$ and $L = \sqrt{2}/k_p$ where k_p is again $k_p = \sqrt{n_0}$.

4

Presentation and discussion of results

In this chapter, all of the results are presented and discussed which are divided into three parts. Section 4.1 cover results from the PIC simulations regarding the amplification of the seed laser. Section 4.2 presents and discusses the analytical result regarding the amplification and frequency-shift of the initial seed field. Lastly, section 4.3 is dedicated to results produced by the custom FDTD code using non-linear wakes and Gaussian density distributions.

4.1 PIC results of 1D LWDA

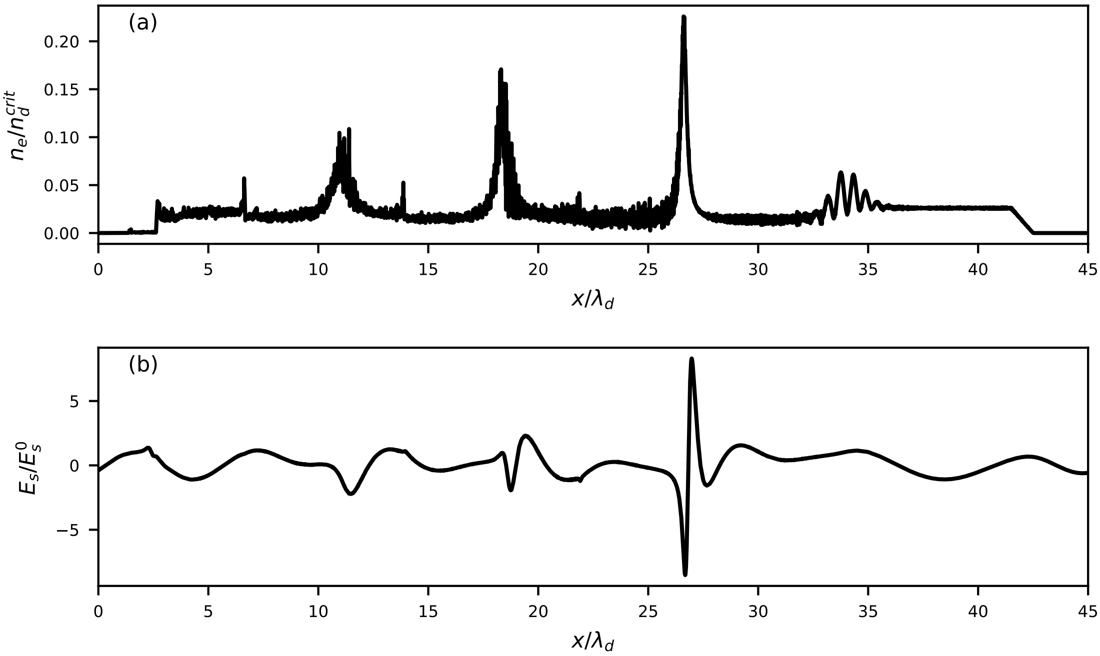

Figure 4.1: PIC simulation of 1D LWDA using normalized driver vector potential $a_d^0 = 2.5$ and seed vector potential $a_s^0 = 0.005$: (a) electron density perturbations normalized to the driver critical density, (b) seed electric field normalized to the initial seed amplitude. This data is taken at a specific time to depict how the most prominent plasma wake is giving rise to the most amplified sub-cycle pulse.

As a start, launching a PIC simulation as presented in section 2.2 will yield amplified sub-cycle pulses which can be examined in figure 4.1. Here the most prominent electron plasma wake is giving rise to the most amplified pulse whereas the other wakefield oscillations modulate other parts of the seed albeit to much lower amplitudes. The amplitude increase is over an order of magnitude as compared to the initial seed amplitude. To determine the frequency up-shift one can take a look at the power spectrum of the sub-cycle train in figure 4.2. To isolate the properties of the most intense sub-cycle pulse, a Super-Gaussian filter has been applied to flatten out any other spectral component, as depicted in the same figure. Here most of the frequency content resides within the broad part of the spectrum peaked around $\sim 9\omega_s$, but there is also a component which lies around $\sim 2.5\omega_s$. This shows that LWDA is possible in 1D as it exhibits similar features as the 2D and 3D investigations made in [15]. For the 2D and PIC simulations of LWDA with the same parameters, the maximum amplification factor was found to be 19. Furthermore, spectral components were found to be up-shifted by 7 times in 2D as compared to the seed frequency.

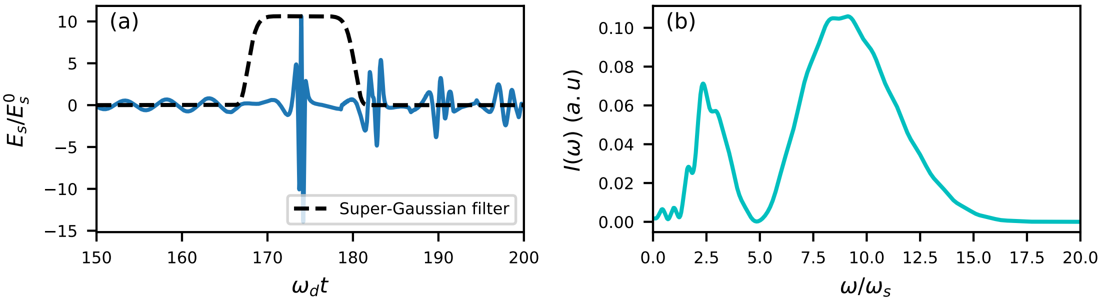

Figure 4.2: (a) Registered seed electric signal as a function of time at the end of the plasma using PIC simulations and a demonstration of where the Super-Gaussian filter is applied, (b) corresponding power spectrum of the filtered signal in (a) normalized to the seed frequency.

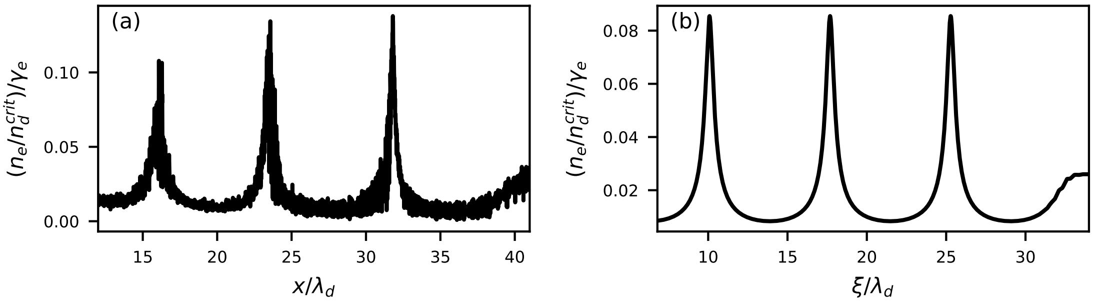

Figure 4.3: Comparison of the n_e/γ_e profile for: (a) PIC simulation using the same parameters as in figure 4.1, (b) non-linear wakefield model using the input parameters presented in section 3.2.2.

Moving on, in figure 4.3 the comparison of the n_e/γ_e profile between that of PIC simulations (a) and the wakefield model (b) can be seen. Plasma waves from the PIC simulation decrease in amplitude for each oscillation whereas the non-linear model maintains the same magnitude for each wave. Overall, the magnitude of the perturbations are similar. Since the profile from the non-linear model agrees with PIC results, this justifies the use of cold fluid theory in the treatment of LWDA. On the other hand, it should be clarified that PIC simulation encapsulates the realistic behavior of plasma wave generation since each density perturbation decreases in amplitude. In the non-linear wakefield model, this is not accounted for and each plasma wave has the same magnitude.

To further validate the use of cold fluid theory in the scope of LWDA, figure 4.4 demonstrates the phase space distribution of 1D LWDA for a given time in the simulation. This shows that the electron plasma has a well defined momentum, i.e. the width of the distribution is small with respect to the maximum momentum. In other words, each spatial point corresponds to one value of longitudinal momentum which confirms the assumption of a Dirac delta distributed fluid momentum made in section 2.1.5. This is very useful since the 1D LWDA PIC results can be used as a reference when discussing the analytical theory or results which are based on cold fluid theory. Lastly, note that the rightmost peaks corresponds to electron momentum attained by the driver laser.

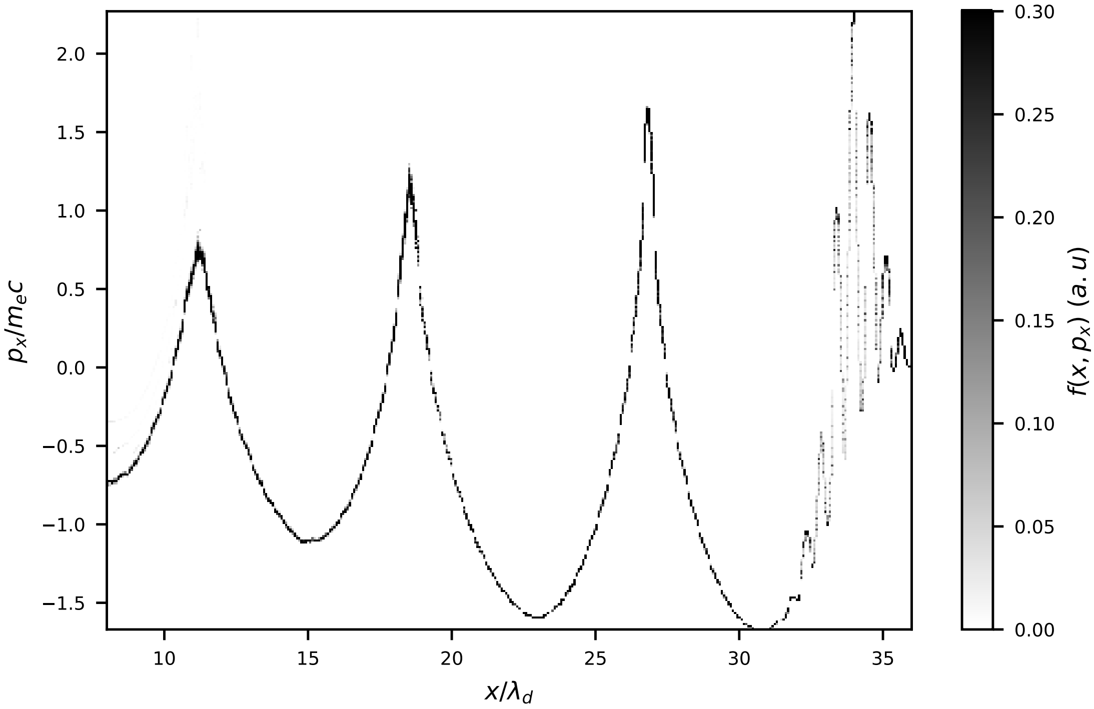

Figure 4.4: PIC simulation of 1D LWDA showing the longitudinal phase space inside the plasma slab for a given time t. This specific time is similar to that of figure 4.1 and uses the same simulation parameters.

4.2 Analytical results

To gain a quantitative understanding as to why laser pulses are amplified by moving density perturbations, one of the theoretical methods was presented in section 3.1 where the analytical calculation was given by making a few assumptions for the laser-plasma interaction. Again, looking at the result (taking the real part of equation (3.14)) of that calculation and comparing it with the incident monochromatic seed laser one finds that

$$E_z(x,t) = \frac{-n_e^{max} a_s^0 t_e \sqrt{\pi}}{2\gamma_e \widetilde{v}^{-1}} \cdot e^{-\frac{(k_s-\omega_s)^2}{4\widetilde{v}^{-2}}} \cdot \cos\left((\omega_s + \frac{k_s - \omega_s}{\widetilde{v}^{-1}})(x-t) \right) \tag{4.1}$$

$$E_s(x,t) = E_s^0 \sin(k_s x - \omega_s t) \tag{4.2}$$

where $E_s^0 = -a_s^0 \omega_s$ is the dimensionless seed laser amplitude and ω_s is the seed laser frequency. Looking at equations (4.1) and (4.2) it is obvious that both of the expressions are monochromatic waves, rather than broadband pulses. However, in the previous section, 1D PIC simulations show that the modulated part of the seed contains an envelope. To explain this, recall figure 4.2(a) which displays the electric field signal at the end of the plasma. Here it is evident that the the amplified pulse has a larger number of cycles as compared to figure 4.1, where the interaction is not yet finished. The longer the seed is allowed to interact with a density perturbation, the larger the number of cycles will be in the amplified pulse. Now, recalling the integration procedure from equation (3.8), it is evident that the interaction proceeds for an indefinite amount of time, as the integration limits extend to infinity. Therefore, an indefinite number of cycles should be produced, losing the pulse envelope in this procedure. This is the reason why expression (4.1) is of CW nature. A possible remedy would be to restrict the density profile to last for a finite amount of time or space which would in turn impact the integration limits. However, this makes the analytical calculation very difficult and requires the need of numerical tools which will reduce the insight gained.

Moving on, the analytical expression suggest that key parameters such as the velocity (which enters $\widetilde{v}^{-1}$ and γ_e), temporal duration t_e and peak magnitude of the density profile n_e^{max} will affect both the amplification and the frequency shift. Another interesting feature is that the seed dispersion relation is crucial in this problem since the expression in (4.1) contains terms of $(k_s - \omega_s)$. Thus, by an appropriate dispersion relation it should be possible to evaluate the frequency and amplitude alterations in this framework. In the simplest case one could try to use the vacuum dispersion relation, $k_s = \omega_s$ and insert this into equation (4.1). Obviously, this is not possible as then both the frequency shift and amplitude modification vanishes and already indicate that refraction plays an important role in this problem. Since the interaction takes place inside a plasma the next option is to use the homogeneous plasma dispersion relation (equation (2.3)) to give an estimate for $k_s = k_s(\omega_s)$. To compare the frequency one can form the following quotient using the normalized values $\omega_s = 0.2$, $\omega_{pe}^2 = n_0 = 0.026$ and $v_\phi = v_g = 0.9869$

$$\frac{\left(\omega_s + \frac{k_s(\omega_s)-\omega_s}{\widetilde{v}^{-1}}\right)}{\omega_s} = \frac{\left(\omega_s + \frac{\sqrt{\omega_s^2-\omega_{pe}^2}-\omega_s}{\widetilde{v}^{-1}}\right)}{\omega_s} \sim 31.8\ . \tag{4.3}$$

Having used the homogeneous dispersion relation it is seen that the frequency is increased more than 30 times as compared to the initial seed frequency.

Further, it is possible to use the same values along with $t_e = 0.21$ and $n_e^{max} = 0.18$ to conclude what the amplification factor is. Forming the quotient between the amplitude in equation (4.1) with E_s^0 gives

$$\frac{\frac{-n_e^{max} a_s^0 t_e \sqrt{\pi}}{2\gamma_e \widetilde{v}^{-1}} \cdot e^{-\frac{(k_s(\omega_s)-\omega_s)^2}{4\widetilde{v}^{-2}}}}{a_s^0 \omega_s} = \frac{-n_e^{max} t_e \sqrt{\pi}}{2\omega_s \gamma_e \widetilde{v}^{-1}} \cdot e^{-\frac{\left(\sqrt{\omega_s^2-\omega_{pe}^2}-\omega_s\right)^2}{4\widetilde{v}^{-2}}} \sim 1.55 \cdot 10^{-4} \tag{4.4}$$

which is a significant reduction in the overall amplitude. By contrast, in the PIC simulations from the previous section spectral components are found to be around 9 times as large compared to the central component of the seed laser. Simulations in [15] found spectral increase within the same order of magnitude in 2D and 3D PIC simulations but never such a large frequency shift as predicted by the analytical expression. For the amplification factor, it appears that using the simulation values in expression (4.4) yields a damped field which is not the case of LWDA. Thus, it appears that the theoretical calculation cannot provide comparable results unless a proper non-linear dispersion relation is provided, which is to this point unknown.

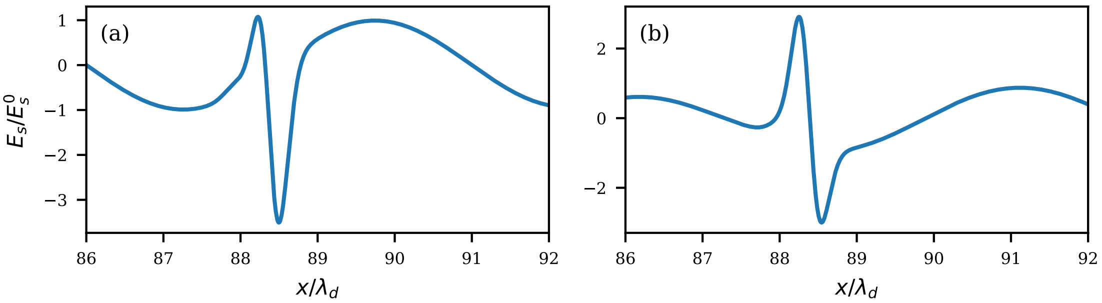

Figure 4.5: Cold fluid simulations demonstrating the modulated part of a seed pulse after the interaction with a Gaussian density distribution: (a) seed field modulation after interacting with a Gaussian density spike having no background plasma, (b) seed field modulation with background plasma $n_b = 0.7n_0$. With the exception of n_b, the common simulation parameters are $n_e^{max} = 0.18$, $v_\phi = v_g = 0.9869$, $t_e = 0.21$ and $\phi_s = 0$.

4.3 Results from custom FDTD cold fluid code

As was discussed in section 3.2.2, it is now possible to simulate how an initial seed laser pulse will be affected by an arbitrary n_e/γ_e profile. In this section, such profiles will be examined in the scope of their ability to compress and amplify the initial seed laser. Further, the CEP tunability and parameteric dependence is also investigated.

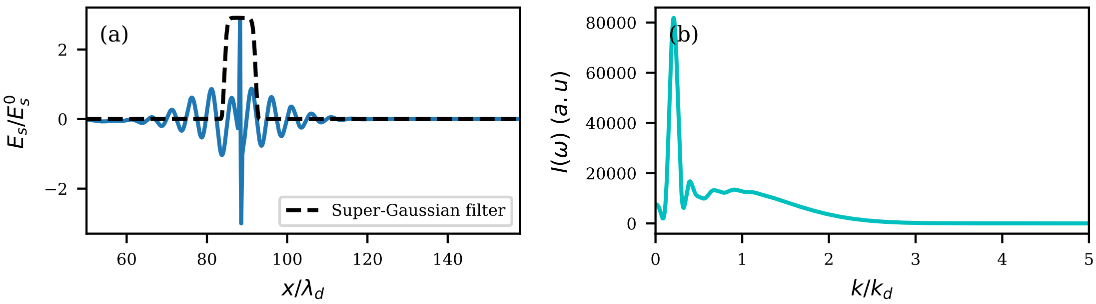

Figure 4.6: Simulation using the cold fluid code to generate the interaction between the seed pulse and a non-evolving Gaussian density spike with background plasma: (a) seed electric field modulation depicted along with a Super-Gaussian filter, (b) corresponding filtered spatial power spectrum.

4.3.1 Gaussian density distribution

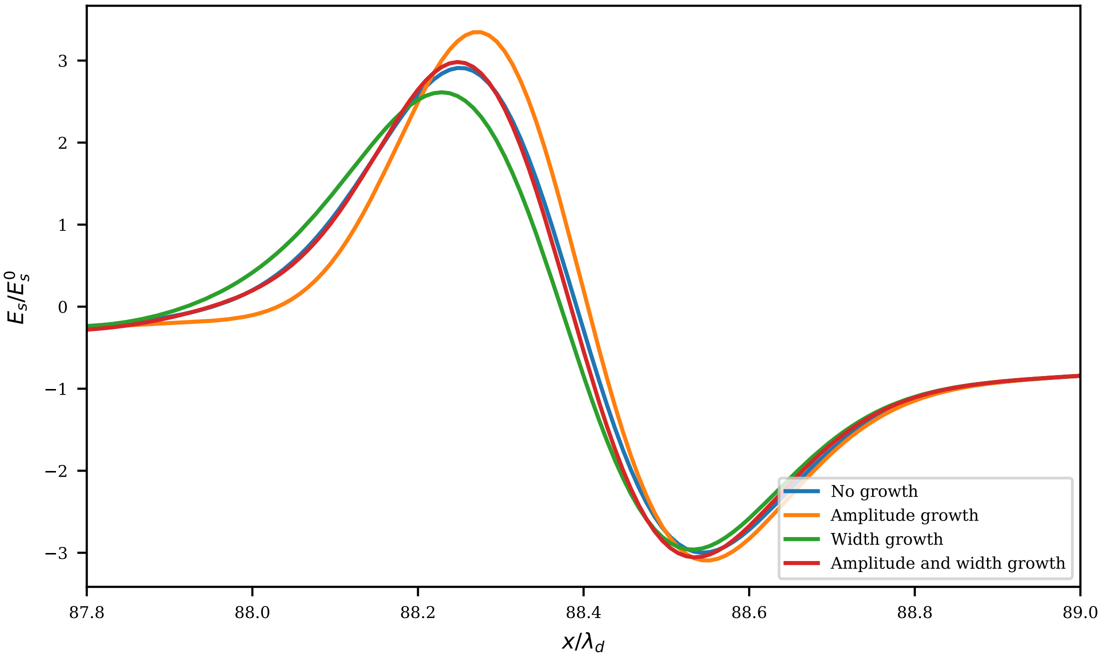

Figure 4.7: Cold fluid simulations depicting the electric field modulation after the interaction of a non-evolving (blue), peak amplitude evolving (yellow), width evolving (green) and both peak amplitude/width evolving (red) density spike.

It is a strong motivation to first look at the laser interaction with a Gaussian density spike as this was used in the analytical framework (see equation (3.12)) and appears to capture well the shape of the density spike in a plasma wave (see e.g. figure 4.1). To begin with, a Gaussian density distribution with constant $\gamma_e = (1 - v_\phi^2)^{-1/2}$ is examined with and without background plasma. This can be viewed in figure 4.5 where the modulated transverse field of the seed is shown after the interaction with said distribution. Having this setting allows the field to be slightly amplified in both cases. However, it is clear that including a background plasma has an impact on the field modulation structure. To justify the use of this ambient plasma, consider figure 4.1(a) where PIC simulations indicate that the electron number density does not go to zero at the end of the density spikes, but rather some background value $n_b \sim 0.7n_0$ where again $n_0 = 0.026$. This in turn also justifies the suggestion from the analytical theory that refraction may be crucial for LWDA.

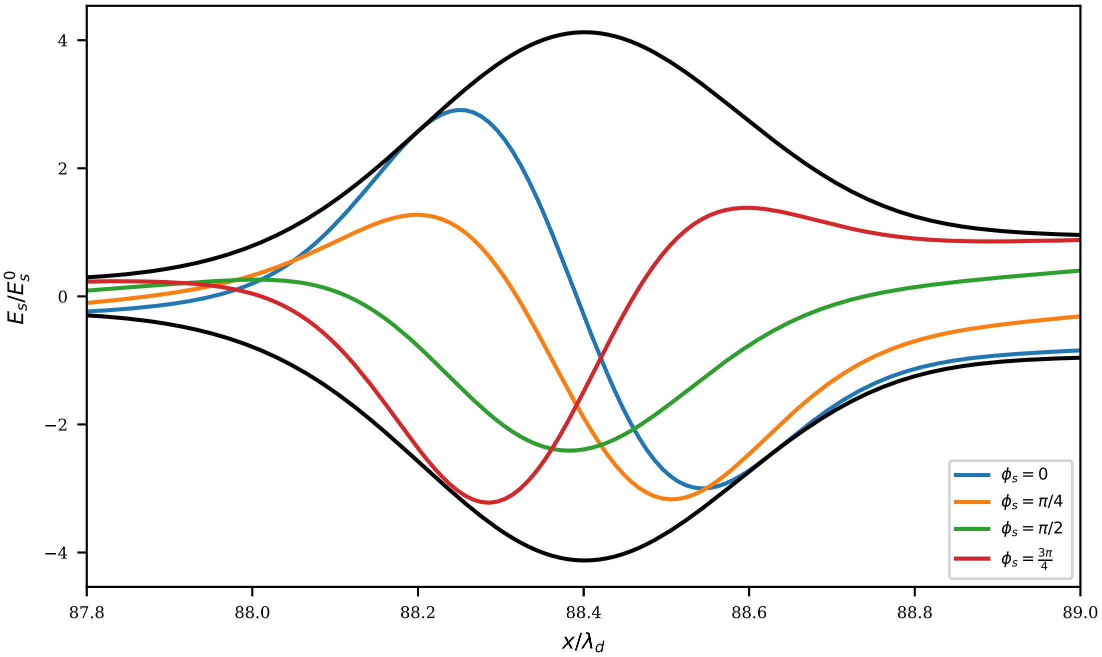

Figure 4.8: Cold fluid code simulation of the interaction between a seed pulse with a non-evolving Gaussian density spike for four different initializations of the seed phase ϕ_s. Every sub-cycle pulse is shown together with a common field envelope (black line) which stems from the standard case $\phi_s = 0$ (blue line).

Moving on, a spatial power spectrum of the electric field signal in figure 4.5(b) can be found in figure 4.6. Here, there are spectral components from the seed fundamental $k = 0.2k_d$ but also that of the modulated part which has a very broad component peaked around $k = 0.9k_d$. From here on, all other simulation results uses a background plasma and will have similar parameters as in figure 4.5.

Next, it is important to examine whether the time-evolution of the peak amplitude and width of the Gaussian electron plasma will have an impact on the compression and amplification of the seed signal. To check this, the distribution (with background plasma) is allowed to have a linear increase in its peak density and decrease in width. In other words, a simulation is started with initial values of $n_e^{max} = 0.18$ and $t_e = 0.21$, which will increase respectively decrease linearly in time by 50% until the end of the simulation. A result for this can be seen in figure 4.7 where the electric field after the interaction with various density spikes is displayed. All types of distributions result in the field modulation having similar structure. In addition to this, having growing density spike yields greater amplification (yellow) and the decrease in width decreases it (green). Having them both evolving together (red) is very similar to the standard, non-evolving case (blue). This agrees to some extent with the analytical theory: increasing n_e^{max} will indeed amplify the seed whereas decreasing t_e will decrease the amplification. Here it should be acknowledged that the analytical theory fails to predict the exact increase respectively decrease as the field modulation does not scale linearly with n_e^{max} and t_e.

Lastly, it is of interest to check if the Gaussian, non-evolving profile will allow to tune the sub-cycle CEP by varying the seed phase. For figure 4.8, simulations were initialized with different phases ϕ_s for the seed laser and the sub-cycle pulse is registered at the end of the simulation. Using this density profile results in no CEP tunability as the different phases ϕ_s have an impact not only on the phase but also on the magnitude of the outgoing pulse.

4.3.2 Non-linear plasma wake distribution

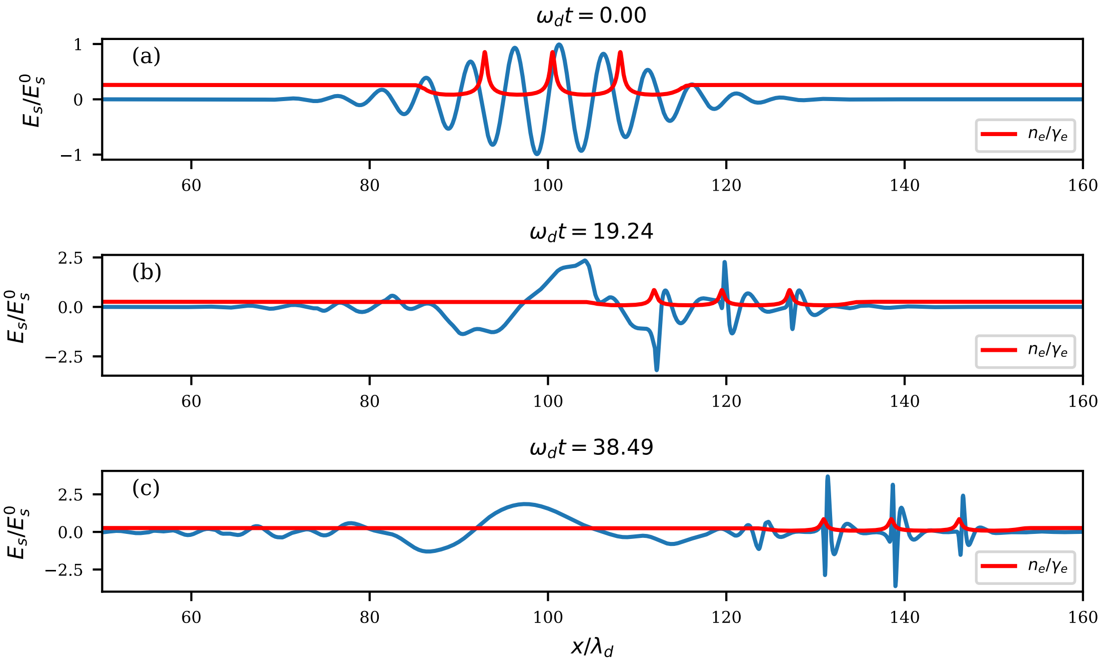

Figure 4.9: Cold fluid simulation result demonstrating the sub-cycle pulse formation when the seed pulse is propagating together with a non-linear plasma wave structure: (a) seed electric field and the n_e/γ_e profile at the beginning, (b) at the middle and (c) at the end of the simulation.

Another approach to model the laser-plasma interaction is to make use of the cold fluid model presented in section 2.1.6 to yield non-linear solutions for the fluid quantities n_e and γ_e which enter equation (3.17). With this in hand, the FDTD code is loaded with said profile and the result is available in figure 4.9 where the seed pulse is propagating to the right along with the electron plasma waves. Evidently, the perturbations is giving rise to one sub-cycle field each and amplifies the laser by a factor of roughly three. This is also in agreement with 1D PIC simulations which display amplification and compression for each density perturbation. By contrast, the overall amplification is roughly one third compared to the amplification predicted by PIC results. It is important to note that there are large reflected components appearing in the simulation. They are also apparent in simulations with Gaussian distributions but are not shown here. This happens whenever the seed laser pulse is instantly initialized into a preformed plasma profile which will introduce reflections or backwards propagating waves. This might have an impact when determining the amplification factor of a specific interaction. If a substantial part of the field is carried away by reflections, the amplification factor could be underestimated. A better approach would be to modify the code in order to fit the PIC simulations better. There, the density perturbations are created over a finite time and do not instantly appear at the simulation initialization. Also the seed laser is allowed to enter the plasma with a ramp up from vacuum which is not the case of the cold fluid code presented in this thesis. However, pursuing such an approach would complicate the model while not altering the basic results significantly.

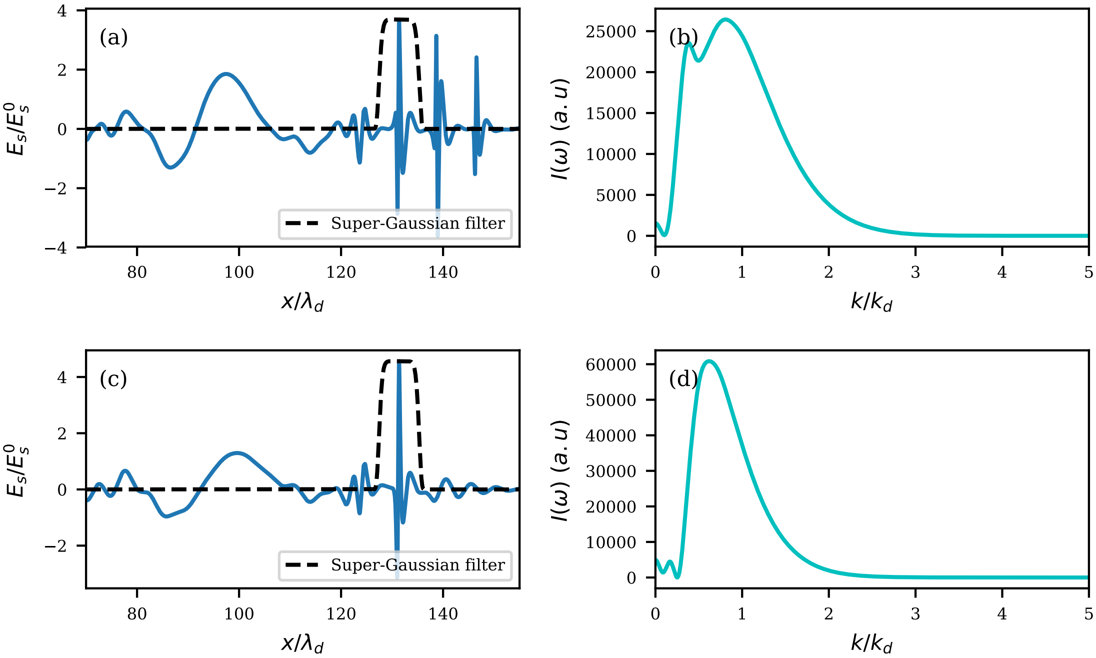

Figure 4.10: Cold fluid simulation using both a single and multiple non-linear plasma wave oscillations as a n_e/γ_e profile: (a,c) seed electric field modulation after the interaction with multiple respectively a single density spike shown together with a Super-Gaussian filter (dashed line), (b,d) corresponding spatial power spectrum of the filtered signal in (a,c) normalized to the driver wavenumber.

It is useful to compare the interaction of the seed pulse with different number of plasma wave oscillations. Thus, in figure 4.10 both the seed electric field modulations and their corresponding filtered power spectra are displayed for interactions with a single and multiple oscillations. Disregarding the fact that each plasma wave period can generate a pulse, the electric field structure is very similar in both cases (a,c). An exception is that the leftmost amplified part of the seed pulse is slightly lower in case (a) as compared to case (c). Due to there being more oscillations and hence more opaque plasma in (a) the reflected component is thus larger than for case (c). This explains why the two differ in terms of amplification since the reflected portion can carry away some of the amplitude. In terms of spectral components, the spatial power spectrum of case (a) appears to peak somewhere around $k \sim 0.8k_d$ whereas case (b) has the major component peaked at $k \sim 0.6k_d$.

Another interesting feature is that this model does exhibit CEP tunability with respect to the seed phase. Figure 4.11 shows how the most amplified sub-cycle pulse CEP differs when using different relative phase of the seed. Clearly, the electric field shape remains within a common envelope regardless of the initial phase of the seed, making it CEP tunable. Compared with figure 4.8 from simulations with a Gaussian plasma distribution with constant γ_e, it seems that the shape of the n_e/γ_e profile based on cold fluid theory will properly capture the CEP dependence. We recall that this choice of profile is further confirmed by PIC simulations due to the good agreement in figure 4.3.

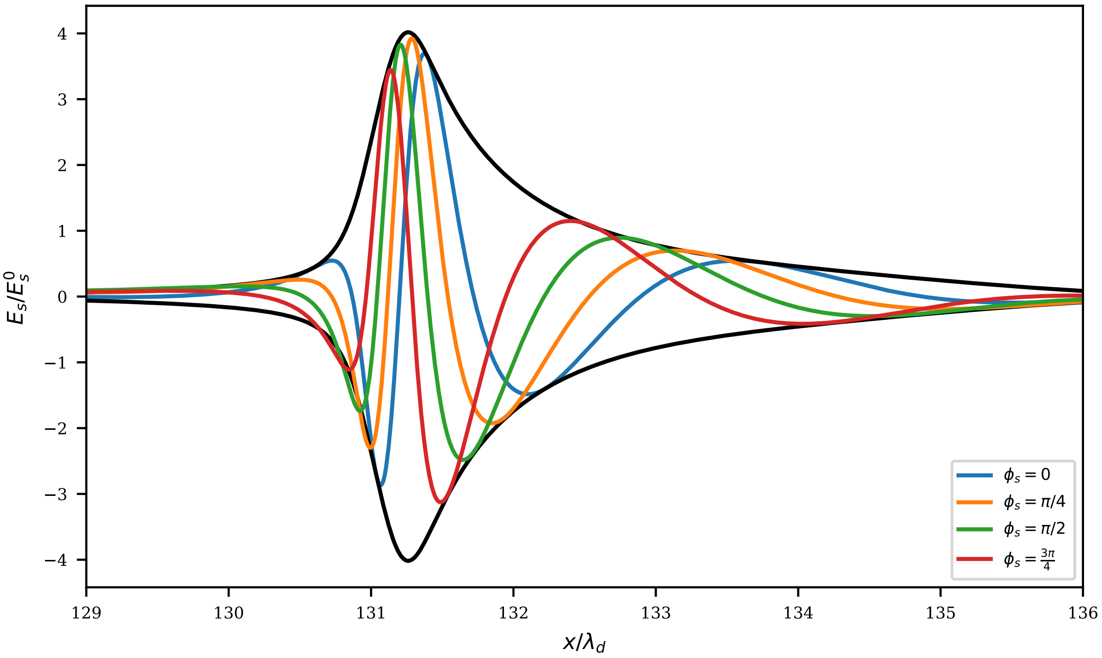

Figure 4.11: Cold fluid simulation results for the interaction of a seed pulse with non-linear plasma waves for four different initializations of the seed phase ϕ_s. Every sub-cycle pulse is shown together with a common field envelope (black line) which stems from the standard case $\phi_s = 0$ (blue line).

5

Conclusion

In this thesis, a 1D analytical theory was developed in order to gain quantitative insights into the sub-cycle pulse generation using LWDA, which has so far been treated in previous works with PIC simulations and qualitative theory. In addition to the theoretical description, a custom code solving Maxwell's equations with a source term from cold fluid theory was written to further understand the underlying mechanism of LWDA. Both methods were compared to 1D PIC simulations.

In the theoretical approach, an expression was obtained which predicts the amplitude change and frequency shift of the outgoing field. According to that expression, parameters such as the peak density, temporal duration and velocity of the Gaussian plasma profile could shift the amplitude and frequency of the seed beam. Furthermore, this also provided an indication that refraction of the seed pulse is important for LWDA as both the seed wavenumber and frequency also appeared in the expression. Nevertheless, it was concluded that the seed dispersion relation is crucial in order to give a full quantitative description of LWDA and that the Green's function method cannot produce comparable results with the simulations.

Simulations with the cold fluid code agreed with 1D PIC simulations since amplified sub-cycle pulses can be generated by having both Gaussian and non-linear plasma-wake n_e/γ_e profiles. However, the latter was favored since it could capture the CEP tunability with respect to the seed phase, in agreement with PIC simulations. In general, the seed amplification for the interaction with a Gaussian and non-linear plasma wakes was lower than what was predicted by 1D PIC simulations. This was also true for their frequency up-shift. However, the change in both amplitude and frequency remained within the same order of magnitude when compared with the 1D PIC results. The reason for this is believed to be that the laser is not properly initialized within the plasma which introduces reflected waves, underestimating the overall amplification. In contrast to the PIC approach, the cold fluid code using a Gaussian density profile was based on the fact that the distribution was non-evolving with a constant γ_e which was not confirmed by PIC simulation nor the non-linear wakefield model. Moreover, the non-linear model, which is a better approximation for the n_e/γ_e profile, is ultimately solved under the quasi-static assumption, meaning that there is no temporal evolution of the non-linear electron waves. This implies that amplification should be reduced compared to PIC, in which the leading density spike amplitude evolves to higher amplitudes during the course of the simulation.

For future investigations, both the analytical theory and the custom cold fluid code could be improved to come even closer to the underlying mechanism of LWDA. PIC simulations demonstrated that γ_e is not entirely constant and perhaps the entire n_e/γ_e structure should enter as a specific function of space and time in equation (3.6). In addition to this, finite interaction time should be considered in forthcoming generalizations of the analytical theory, as this should lead to amplified pulses of proper duration. Moreover, the custom code should be improved to reduce the reflected components when interacting with n_e/γ_e distributions. Thus, the seed pulse should not be loaded into the profile instantaneously but rather enter the plasma slab from vacuum and perhaps the density spike could be formed slowly over a finite time. Lastly, it would be interesting to have an extended study of the parameter space for LWDA using the cold fluid code.

In conclusion, this thesis has developed a quantitative model for the scheme of LWDA. Models based on cold fluid theory has shown that indeed amplification and compression of electromagnetic pulses can be achieved with both Gaussian and plasma wake n_e/γ_e profiles. The latter model captures the interaction more faithfully than the former, both qualitatively and quantitatively. Most importantly, interactions with non-linear plasma wakes could capture the CEP invariance when tuning the seed phase, in good agreement with PIC results.

Bibliography

[1] Hohenleutner et al., “Real-time observation of interfering crystal electrons in high-harmonic generation,” Nature, vol. 523, no. 7562, pp. 572–575, Jul. 2015, doi: 10.1038/nature14652.

[2] P. B. Corkum and F. Krausz, “Attosecond science,” Nature Phys, vol. 3, no. 6, pp. 381–387, Jun. 2007, doi: 10.1038/nphys620.

[3] U. Morgner et al., “Sub-two-cycle pulses from a Kerr-lens mode-locked Ti:sapphire laser,” Opt. Lett., vol. 24, no. 6, p. 411, Mar. 1999, doi: 10.1364/OL.24.000411.

[4] C. Manzoni et al., “Coherent pulse synthesis: towards sub-cycle optical waveforms: Coherent pulse synthesis: towards sub-cycle optical waveforms,” Laser Photonics Reviews, vol. 9, no. 2, pp. 129–171, Mar. 2015, doi: 10.1002/lpor.201400181.

[5] I. Thiele, E. Siminos, and T. Fülöp, “Electron beam driven generation of frequency-tunable isolated relativistic sub-cycle pulses,” Phys. Rev. Lett., vol. 122, no. 10, p. 104803, Mar. 2019, doi: 10.1103/PhysRevLett.122.104803.

[6] L. Plaja, L. Roso, K. Rzazewski, and M. Lewenstein, “Generation of attosecond pulse trains during the reflection of a very intense laser on a solid surface,” J. Opt. Soc. Am. B, vol. 15, no. 7, p. 1904, Jul. 1998, doi: 10.1364/JOSAB.15.001904.

[7] D. von der Linde et al., “Generation of high-order harmonics from solid surfaces by intense femtosecond laser pulses,” Phys. Rev. A, vol. 52, no. 1, pp. R25–R27, Jul. 1995, doi: 10.1103/PhysRevA.52.R25.

[8] S. Kohlweyer, G. D. Tsakiris, C.-G. Wahlström, C. Tillman, and I. Mercer, “Harmonic generation from solid-vacuum interface irradiated at high laser intensities,” Optics Communications, vol. 117, no. 5–6, pp. 431–438, Jun. 1995, doi: 10.1016/0030-4018(95)00200-R.

[9] D. an der Brügge and A. Pukhov, “Enhanced relativistic harmonics by electron nanobunching,” Physics of Plasmas, vol. 17, no. 3, p. 033110, Mar. 2010, doi: 10.1063/1.3353050.

[10] A. A. Gonoskov, A. V. Korzhimanov, A. V. Kim, M. Marklund, and A. M. Sergeev, “Ultrarelativistic nanoplasmonics as a route towards extreme-intensity attosecond pulses,” Phys. Rev. E, vol. 84, no. 4, p. 046403, Oct. 2011, doi: 10.1103/PhysRevE.84.046403.

[11] A. Gonoskov, “Theory of relativistic radiation reflection from plasmas,” Physics of Plasmas, vol. 25, no. 1, p. 013108, Jan. 2018, doi: 10.1063/1.5000785.

[12] C. Hernández-García et al., “Zeptosecond High Harmonic keV X-Ray Waveforms Driven by Midinfrared Laser Pulses,” Phys. Rev. Lett., vol. 111, no. 3, p. 033002, Jul. 2013, doi: 10.1103/PhysRevLett.111.033002.

[13] G. D. Tsakiris, K. Eidmann, J. Meyer-ter-Vehn, and F. Krausz, “Route to intense single attosecond pulses,” New J. Phys., vol. 8, pp. 19–19, Jan. 2006, doi: 10.1088/1367-2630/8/1/019.

[14] T. Baeva, S. Gordienko, and A. Pukhov, “Theory of high-order harmonic generation in relativistic laser interaction with overdense plasma,” Phys. Rev. E, vol. 74, no. 4, p. 046404, Oct. 2006, doi: 10.1103/PhysRevE.74.046404.

[15] E. Siminos and I. Thiele, “Laser wakefield driven generation of isolated CEP-tunable intense sub-cycle pulses,” arXiv:1902.05014v3 [physics], Oct. 2019, Accessed: Apr. 03, 2020. [Online]. Available: http://arxiv.org/abs/1902.05014v3.

[16] G. Günter et al., “Sub-cycle switch-on of ultrastrong light–matter interaction,” Nature, vol. 458, no. 7235, pp. 178–181, Mar. 2009, doi: 10.1038/nature07838.

[17] T. Rybka, M. Ludwig, M. F. Schmalz, V. Knittel, D. Brida, and A. Leitenstorfer, “Sub-cycle optical phase control of nanotunnelling in the single-electron regime,” Nature Photon, vol. 10, no. 10, pp. 667–670, Oct. 2016, doi: 10.1038/nphoton.2016.174.

[18] D.Anderson, M.Lisak, P.Johannisson and M.Marklund, "Basic Plasma Physics - Theory and Applications". Gothenburg, Sweden, 2003.

[19] J. Magnusson, Chalmers tekniska högskola, and Department of Physics, Intense laser-plasma interactions. 2019.

[20] A. Macchi, A superintense laser-plasma interaction theory primer. Dordrecht: Springer, 2013.

[21] J. D. Jackson, Classical electrodynamics, 3rd ed. New York: Wiley, 1999.

[22] E. Esarey, A. Ting, P. Sprangle, D. Umstadter, and X. Liu, “Nonlinear analysis of relativistic harmonic generation by intense lasers in plasmas,” IEEE Trans. Plasma Sci., vol. 21, no. 1, pp. 95–104, Feb. 1993, doi: 10.1109/27.221107.

[23] E. Esarey, C. B. Schroeder, and W. P. Leemans, “Physics of laser-driven plasma-based electron accelerators,” Rev. Mod. Phys., vol. 81, no. 3, pp. 1229–1285, Aug. 2009, doi: 10.1103/RevModPhys.81.1229.

[24] P. Sprangle, E. Esarey, and A. Ting, “Nonlinear theory of intense laser-plasma interactions,” Phys. Rev. Lett., vol. 64, no. 17, pp. 2011–2014, Apr. 1990, doi: 10.1103/PhysRevLett.64.2011.

[25] P. Sprangle, E. Esarey, and A. Ting, “Nonlinear interaction of intense laser pulses in plasmas,” Phys. Rev. A, vol. 41, no. 8, pp. 4463–4469, Apr. 1990, doi: 10.1103/PhysRevA.41.4463.

[26] T. D. Arber et al., “Contemporary particle-in-cell approach to laser-plasma modelling,” Plasma Phys. Control. Fusion, vol. 57, no. 11, p. 113001, Nov. 2015, doi: 10.1088/0741-3335/57/11/113001.

[27] J. Derouillat et al., “Smilei": A collaborative, open-source, multi-purpose particle-in-cell code for plasma simulation,” Computer Physics Communications, vol. 222, pp. 351–373, Jan. 2018, doi: 10.1016/j.cpc.2017.09.024.

[28] A. Taflove, Computational electrodynamics: the finite-difference time-domain method. Boston: Artech House, 1995.

[29] Y.D.Chong, "Green's functions", 2016. Accessed on: May 28, 2020. [Online]. Available: `http://www1.spms.ntu.edu.sg/~ydchong/teaching/10_greens_function.pdf`

[30] G. B. Arfken and H.-J. Weber, Mathematical methods for physicists, 4th ed. San Diego: Academic Press, 1995.

[31] V. I. Berezhiani and I. G. Murusidze, “Interaction of highly relativistic short laser pulses with plasmas and nonlinear wake-field generation,” Phys. Scr., vol. 45, no. 2, pp. 87–90, Feb. 1992, doi: 10.1088/0031-8949/45/2/007.

[32] Bulanov, S. V., V. I. Kirsanov, and A. S. Sakharov, "Excitation of ultrarelativistic plasma waves by pulse of electromagnetic radiation," JETP Lett 50, no. 4 (1989): 198-201.